Published in IEEE Access with doi: 10.1109/ACCESS.2024.3372412

Circle Search Algorithm-Based Super Twisting Sliding Mode Control for MPPT of Different Commercial PV Modules

Ghazi A. Ghazi [1, 2]*, Essam A. Al-Ammar [1], Hany M. Hasanien [3], and Rania A. Turky [4], Marcos Tostado-Véliz[5], and Francisco Jurado[5]

[1] Department of Electrical Engineering, College of Engineering, King Saud University, P.O. Box 800, Riyadh 11421, Saudi Arabia; (e-mail: 439106681@student.ksu.edu.sa; essam@ksu.edu).

[2] K.A.CARE Energy Research and Innovation Center, King Saud University, Riyadh 11421, Saudi Arabia

[3] Electrical Power and Machines Department, Faculty of Engineering, Ain Shams University, Cairo 11517, Egypt; (e-mail: hanyhasanien@ieee.org)

[4] Electrical Engineering Department, Faculty of Engineering and Technology, Future University in Egypt, Cairo 11835, Egypt; (e-mail: rania.turky@fue.edu.eg)

[5] Department of Electrical Engineering, University of Jaén, 23700 Linares, Spain. (e-mail: mtostado@ujaen.es ; fjurado@ujaen.es).

Abstract

The efficiency of grid-connected photovoltaic (PV) systems can be improved using a suitable maximum power point tracking (MPPT) control. Many MPPT techniques have been developed. However, when atmospheric conditions change rapidly, the PV modules respond nonlinearly and the performance of these methods especially the conventional ones is significantly reduced. Therefore, to successfully pursue the maximum power point (MPP) in PV systems, a robust MPPT integrated with sliding mode control (SMC) is employed. This paper proposes a circle search algorithm based super twisting SMC (CSA-STSMC) for tracking the MPP for 100-kW of different commercial grid-connected PV modules coupled with an energy storage system that used to smooth their output fluctuations. Moreover, the STSMC and PI controllers' gains are optimized using the CSA and Grey Wolf Optimizer (GWO) methods and the performance of proposed method is demonstrated through comparisons with the CSA-PI and the GWO-STSMC methods. The optimization and simulation analysis are executed in A MATLAB/Simulink environment. It is observed that the proposed method outperforms the considered methods in terms of robustness, tracking speed, best convergence to the minimum error's value and better tracking efficiency in the maximizing the extracted power from the introduced PV systems.

Keywords: Circle search algorithm, Grey wolf optimizer, Maximum power point tracking, Photovoltaic system, PI controller, Super twisting sliding mode controller.

1. Introduction

1.1. Background

Because traditional fossil fuel energy has been quickly depleting, renewable energy sources (RESs) are now crucial. Thanks to improvements in semiconductor materials and cost reduction, as well as the sustainability, availability, and environmentally friendly nature of solar energy, PV generation has had the fastest growth among RESs [1]. The renewable energy policy network for the 21st century (REN21) estimates that 942 GW of installed PV power was presented globally in 2022, an increase of more than 20% from 2021 [2]. However, the amount of solar radiation and ambient temperature significantly impact much energy generated by PV systems [3]. Additionally, solar irradiance level and cell temperature affect the PV array's current and voltage. [4]. As a result, the PV cell's current changes with solar irradiance level, and PV voltage trails the temperature evolution. Therefore, an interface between PV systems and a utility grid or local load is necessary for maximum power transfer. Typically, an efficient maximum power point tracking (MPPT) method is required to control the duty cycle of a power electronics circuit, such as a DC-DC boost converter [5]. Additionally, a DC-AC inverter, a power electronics circuit, is utilized to connect a PV system to the grid and transform the DC power into AC power that can be fed safely into the grid.

1.2. Literature review

Extensive study has previously been done on this topic to boost the efficiency of PV systems by adopting tracking methodologies for MPP. A trustworthy control keeps tracking the MPP in all environmental circumstances and forces the system to function at its best. There have been several different MPPT techniques developed over the past two decades, including perturb and observe (P&O) [6], incremental conductance (INC) [7], hill-climbing (HC) [8], fractional open-circuit voltage (FOV) [9], and fractional short-circuit current (FSC) [10], In addition, the MPP has been effectively tracked utilizing intelligent techniques including fuzzy logic controller (FLC) [11], artificial neural network (ANN) and genetic algorithm (GA) [12].

Furthermore, an extensive research has revealed a strong interest in metaheuristic MPPTs in a variety of environmental conditions including a particle swarm optimization (PSO) [13], an improved chaotic PSO (ICPSO) [14], firefly algorithm (FA) [15], grey wolf optimization technique (GWO) [16], slime mould optimization (SMO) [17], an improved artificial bee colony (ABC) technique [18], an ant colony optimizer (ACO) [19], cuckoo search algorithm (CSA) [20], and salp-swarm optimization (SSO) [21]. The intermittent nature of the irradiance level can cause fluctuations in the PV systems' output power. Those power fluctuations must be reduced before the power is transferred to the grid. As a result, many techniques, including storage devices, have been employed to smooth the output power of RESs systems. The output power of RESs can be adequately smoothed using battery-storage devices [22]. Multiple variants of MPPT methods are published in the literature, with differences in accuracy tracking, complexity, cost-effectiveness range, and convergence speed.

Sliding mode control has become quite popular owing to its advantages in the design of nonlinear control systems, including its robustness, simplicity, and good dynamic behavior. Due to these attributes, the demand for SMC has increased for implementing MPPT systems [23]. It has been utilized to overcome parametric variations and unknown

external and internal disturbances in a variety of control systems, including robotics [24], inverter control systems [25], and motor controls [26]. It is desirable to use a nonlinear control technique to pursue MPP since PV systems exhibit nonlinear behavior. In this regard, several novel MPPT algorithms based on SMC have been implemented including current sensor based SMC [27], first order SMC [28], P&O based fractional SMC [29], INC based SMC [30], backstepping SMC [31], improved double integral SMC [32], fast terminal SMC-based direct power control [33], fuzzy neural network approach based terminal SMC [34], double integral SMC [35], second order SMC [36] , super twisting SMC [37], and PSO-based SMC [38].

Summarizing the literature on MPPT-based SMC above, it can be found that the first-order SMC-MPPTs [27], [28] have the qualities of being robust and straightforward, and they can be easily implemented in hardware. Nevertheless, they exhibit chattering issues and do not reveal good dynamics during rapid-changing environmental conditions. The P&O-based SMC [29] takes over the characteristics of the traditional one, and the reference generated is tracked by SMC. However, this approach lacks the trajectory's adaptability, speed, and losses, particularly in varying weather conditions. The INC-SMC method [30] demonstrated a quick dynamic response under fluctuating irradiance and temperature levels. Conversely, producing the reference signal requires quick PV curve slope computation and has shown oscillations in steady-state situations.

The curve fitting methods [31], [32] are implemented to search for the reference signals in the linear polynomial expressions. These methods are quick in the estimation of reference signals. However, these expressions lack generality and module specificity. Terminal SMC [33], [34], double integral SMC[35], super twisting theorem-based SMC [36], [37], and artificial intelligence algorithm-based SMC [38] are examples of advanced versions of SMC. These sophisticated versions are more expensive than conventional ones because they need rapid processing resources to do complex calculations. On the other hand, their benefits include rapid convergence, negligible oscillations, and precise MPP tracking in steady-state and rapidly changing settings.

1.3. Main contributions

A solar cell's characteristic depends on the irradiance level, temperature, and array voltage. Therefore, an MPPT is needed to move the operating voltage near the MPP under different atmospheric conditions. A proper MPPT control method should be applied with a DC-DC boost converter to guarantee its stability regardless of operating conditions. The circle search algorithm (CSA) is a recently developed metaheuristic algorithm in which the main advantages are its straightforward process, reduced computational load, and minimal design requirements. Various engineering problems have been solved using this algorithm, like estimating solar modules using a three-diode model [39] and optimizing the PEM fuel cell model [40]. This paper proposes CSA based super twisting SMC for MPPT of five different commercial PV modules (Amorphous silicon (ASi), Cadmium Telluride (CdTe), and Copper Indium Selenium (CIS), Monocrystalline silicon (McSi), and Polycrystalline silicon (PcSi)). In this work, after finding the optimal gain parameters of both STSMC and PI controllers of PV and energy storage systems (ESSs) using the CSA and GWO methods, the CSA method is then utilized for tracking the MPP and producing a reference signal (voltage/current). At the same time, the STSMC is used to regulate the measured signal about this reference signal. Additionally, the STSMC’s output is connected to pulse width modulation (PWM) to produce the corresponding duty

cycles of the DC boost converter. Also, another STSMC is used to regulate the battery current concerning a battery reference current. Also, the STSMC's output is connected to two PWMs to produce the corresponding duty cycle of the buck-boost converter for optimal charge and discharge of the ESS. The significant contributions of this work are as follows:

- Evaluating five different commercial PV modules in harsh weather conditions.
- Modeling two sliding mode controllers for boost and buck-boost converters.
- Proposing a circle search algorithm-based super twisting SMC for MPPT of PV systems.
- Tuning the gain parameters of super twisting SMCs (three for boost converter and three for buck-boost converter) using the CSA.
- Compare the proposed method's results with CSA-PI and GWO-STSMC methods.
- Also, tuning the gain parameters of PI and STSMC controllers using the CSA and GWO methods.
- Proposing a storage system to smooth the fluctuation in the PV system's produced power.

The rest of the paper is structured this way: the proposed system's modeling is provided in Section 2. The methodology, including the objective equations and the proposed CSA method, are described in Section 3. The results and discussions are illustrated in Section 4. Finally, the conclusions are provided in Section 5.

2. System Modeling

The proposed system under study is depicted in a block diagram in Figure 1. The PV array's measured signal (voltage/current) is regulated with respect to a reference voltage/current produced by the proposed MPPT-based STSMC by modifying the duty cycles of the DC boost converter. Additionally, the charge and discharge operations of the storage system are managed by a buck-boost converter. In the storage system, the STSMC regulates the battery current concerning a reference one and is linked to PWM to produce the correct duty cycles for the buck-boost converter. The PV system, along with ESS that is utilized to smooth out the fluctuations in its output power, is connected to a DC to AC inverter, which enables the PV system to be interconnected with the grid and convert the DC power into AC power to be injected into the utility grid,

2.1 PV system modeling

The proposed on-grid PV system with a capacity of 100 kW is demonstrated in Figure 1 for different commercial PV modules. The data of the proposed system are specified in appendix A (Table A.1) [41]. This system involves a PV array made up of several connected parallel and series PV modules. The PV array's terminal is connected to a boost converter (its data is given in Table A.2) . Furthermore, the PV system's MPP is controlled by modifying the duty cycles of the DC boost converter, which is used to increase the efficiency of the PV system and regulates the array's terminal voltage thereby transmits the maximum power to a DC link linked to a utility grid through DC to AC inverter. The PV array's inputs are solar irradiance and temperature curves, as shown in Figures 4 and 5. These inputs were taken from a weather-monitoring station at King Saud University, Riyadh, Saudi Arabia (on 12/01/2020). In addition, Figures 6 and 7 show the PV array's P–V and I–V characteristic curves under standard (solar irradiance level is 1000

W/m^2 and temperature is 25 C^o) and non-standard test conditions (actual data), respectively. Equation (5) of the PV array's output current is obtained as follows:

From Figure 2, which represents a circuit single-diode diagram of a PV cell, the diode current I_D can be computed as follows [42], [43]:

$$I_D = I_o(\exp(\frac{q(V_{pv} + R_s I_{pv})}{AkT})) \quad (1)$$

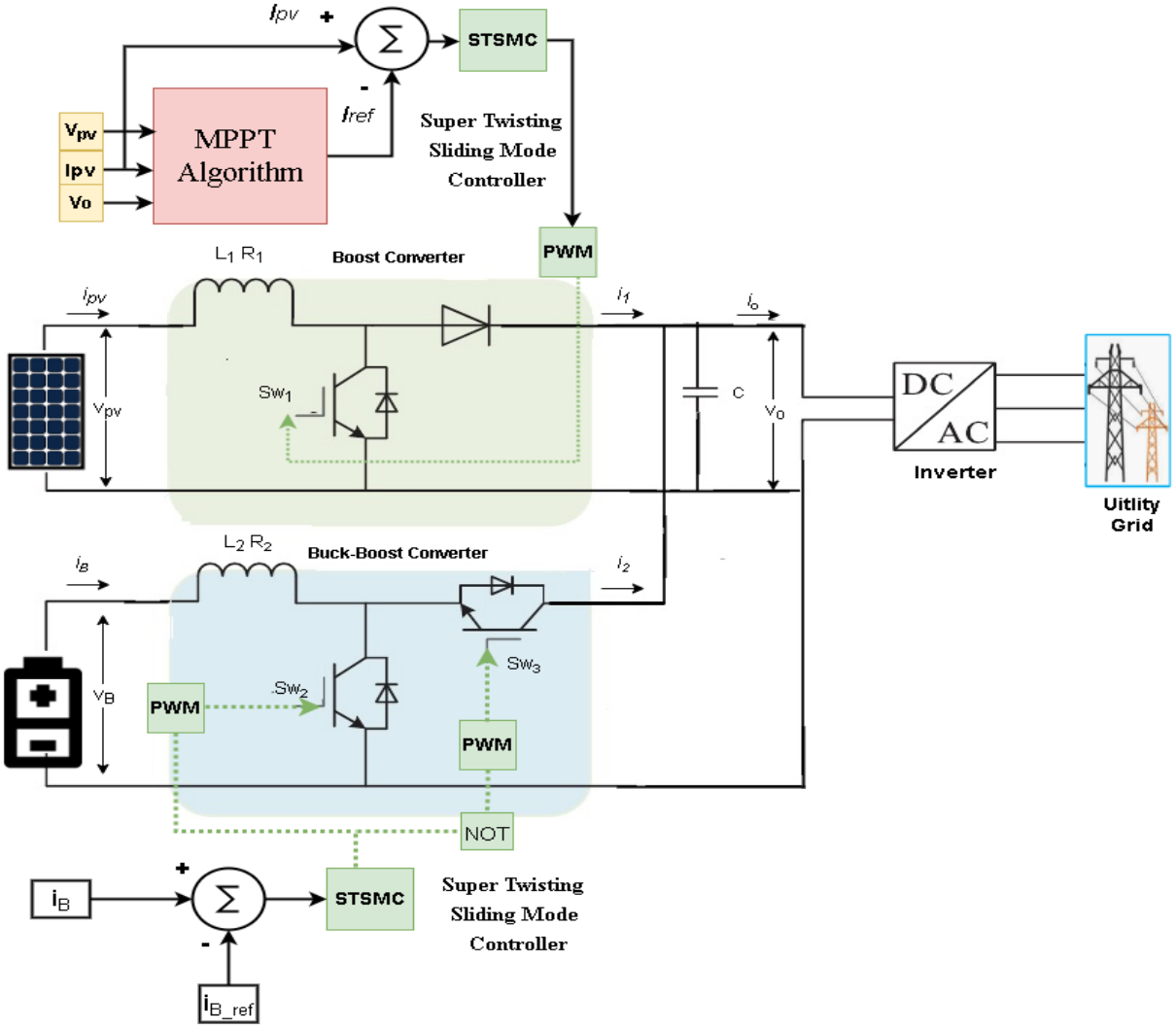

Figure 1. Circuit topology of the proposed system

Here, I_o is the saturation current, V_{pv} and I_{pv} are PV cell's output voltage and current, respectively, R_s is the series resistance, q is the electronic charge ($q = 1.6 \times 10^{-19}$ C), A is the diode ideality factor, k is the Boltzmann constant, and T (Kelvin) is the ambient temperature of the PV cell.

As displayed in Figure 2, the output current (I_{pv}) produced by the PV cell, according to Kirchhoff's current law, can be characterized as follows:

$$I_{pv} = I_s - I_o\left(\exp\left(\frac{q(v_{pv} + R_s i_{pv})}{AkT}\right) - 1\right) - \frac{v_{pv} + R_s i_{pv}}{R_{sh}} \quad (2)$$

Here, I_s is the photocurrent and R_{sh} is the shunt resistor.

The photocurrent current I_s can be specified as follows:

$$I_s = (I_{sc} - k_i(T - T_{ref}))\frac{G}{G_{ref}} \quad (3)$$

Here, I_{sc} is the cell short-circuit current, k_i is the short-circuit current coefficient, G and G_{ref} are the operating and reference solar radiations, and T and T_{ref} are the ambient and reference temperatures, respectively.

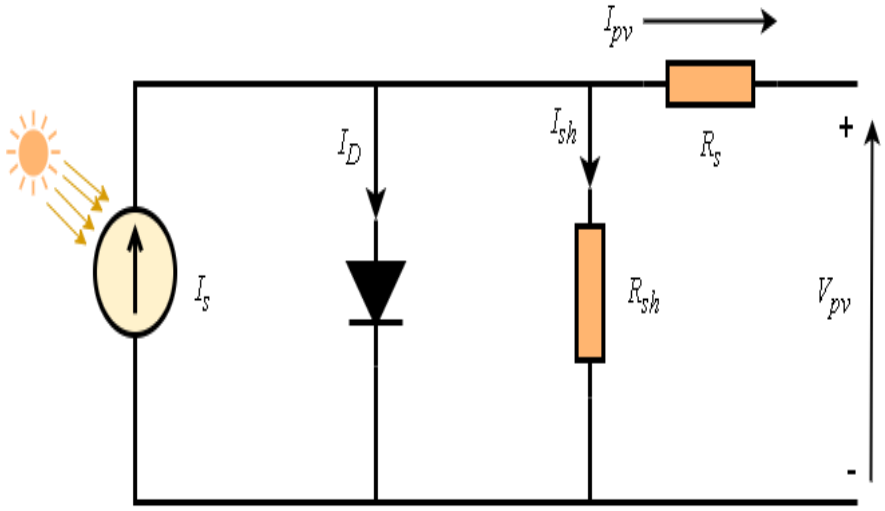

Figure 2. Circuit of single-diode diagram of a PV cell

The saturation current I_o can be computed as follows:

$$I_o = I_{Rs}\left(\frac{T}{T_{ref}}\right)^3 \exp\left(\frac{qE_g}{Ak}\left(\frac{1}{T_{ref}} - \frac{1}{T}\right)\right) \quad (4)$$

Here, E_g is the semiconductor's energy gap and I_{Rs} is the reverse-saturation current at a reference solar irradiation level and temperature.

Figure 3 shows PV modules that are linked in series (N_s) and in parallel (N_p) to make a PV array. Thus, the output PV array current (I_{pv})can be found as follows:

$$I_{pv} = N_s\, I_s - N_p I_o\left(\exp\left(\frac{q(V_{pv} + R_s I_{pv})}{AkTN_s}\right) - 1\right) - N_p\frac{V_{pv} + R_s I_{pv}}{N_s R_{sh}} \quad (5)$$

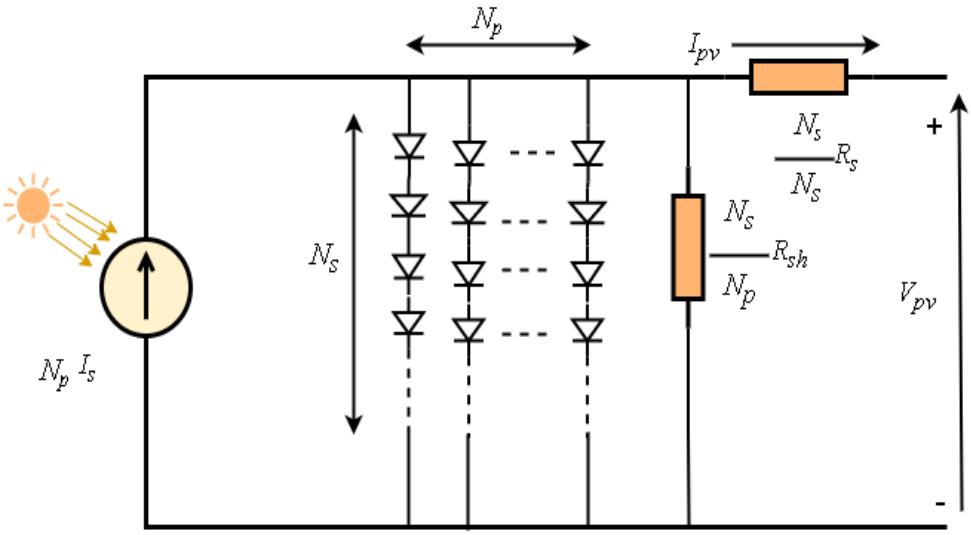

Figure 3. Circuit diagram of a PV array.

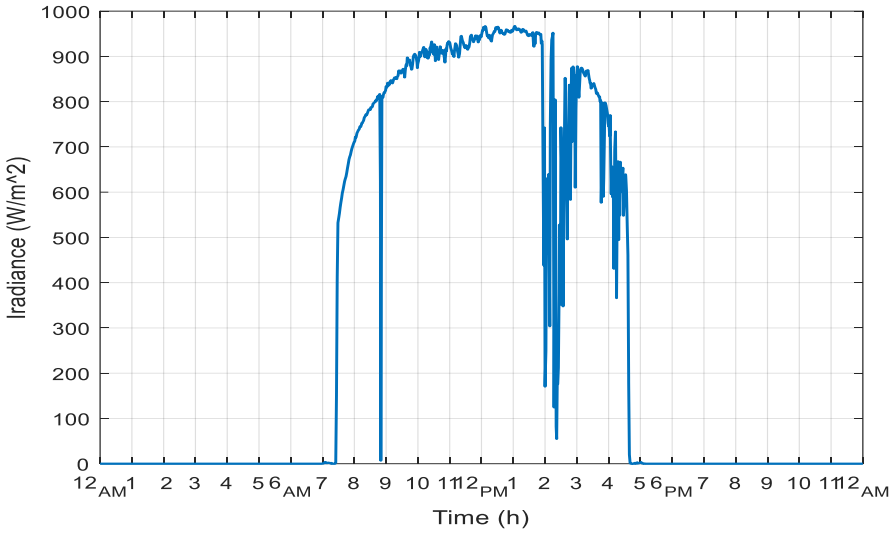

Figure 4. Solar irradiance.

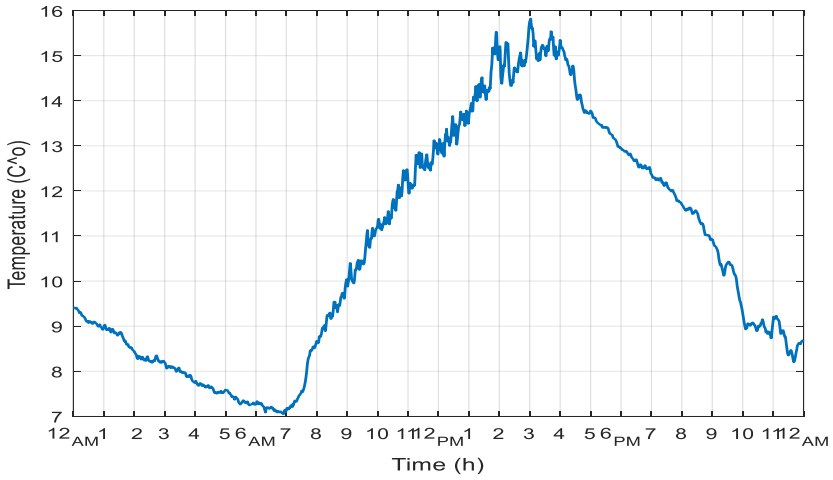

Figure 5. Temperature.

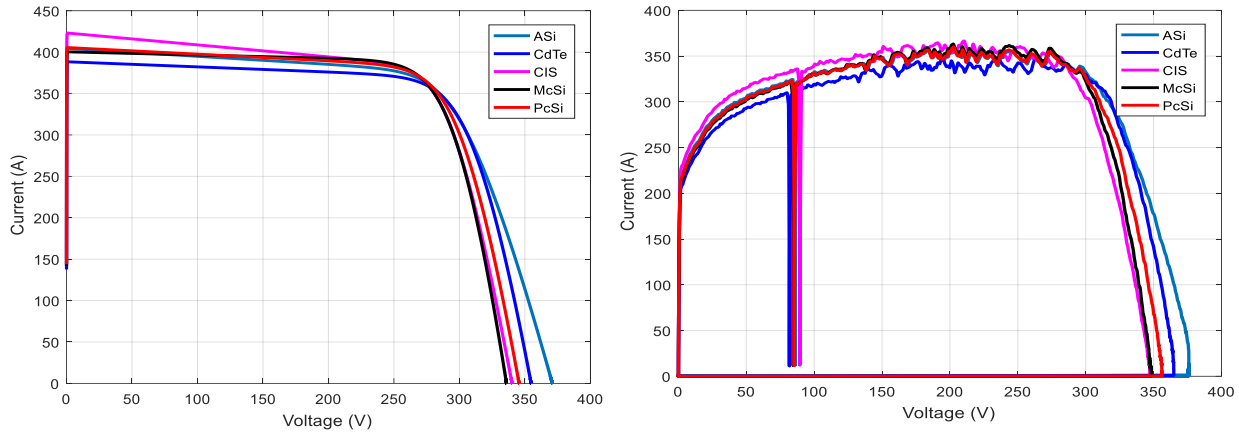

(a) (b)

Figure 6. I-V characteristic curves for different modules; (a) under standard test conditions, (b) under non-standard test conditions.

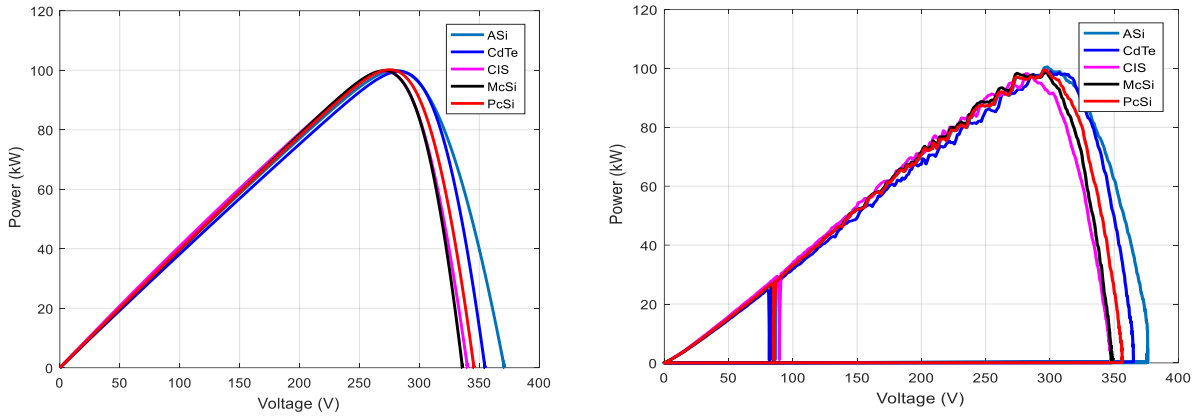

(a) (b)

Figure 7. P-V characteristic curves for different modules; (a) under standard and (b) non-standard test conditions.

2.2 Boost converter modeling

The DC boost converter can step up its input voltage magnitude. In addition, the boost converter consists of an IGBT switch, a diode, a capacitor, an inductor, and resistance. Therefore, it functions when the IGBT switch is fired during the ON state and turned off during the OFF state. The dynamic equations can be obtained by utilizing Kirchhoff's law to the part of the PV system and boost converter as follows [44]:

$$\frac{dI_{pv}}{dt} = \frac{V_{pv}}{L_1} - \frac{R_1 I_{pv}}{L_1} - \frac{V_o}{L_1}(u_1 - 1) \tag{6}$$

$$I_1 = (1 - u_1) I_{pv} \tag{7}$$

Where L_1 and R_1 represent inductance and resistance of the boost converter, and the symbol u_1 is the duty cycle of the IGBT S_{w1} ranges from 1 to 0.

2.3 Buck-boost converter modeling

The bidirectional buck-boost converter can step up or down its input voltage depending on its duty cycle. Additionally, taking into account the storage system's properties, its auxiliary operation can be split into discharge and charge states. If the battery works in a discharged state, u_3, which is the duty cycle of the IGBT S_{w3} of the buck-boost converter is limited to 0 while u_2, which is the duty cycle of the IGBT S_{w2}, takes a value range from 1 to 0. When it on the charge state, u_2 is set to 0, and u_3 ranges from 1 to 0. The charge state can be expressed mathematically as follows [44]:

$$\dot{I}_B^* > 0$$

$$\frac{dI_B}{dt} = \frac{1}{L_2}V_B - \frac{R_2}{L_2}I_B - \frac{(1-u_2)}{L_2}V_o \tag{8}$$

Here, $\dot{I}_{L_2}^*$ is the battery reference current.

The discharge state of the battery can be expressed mathematically as follows:

$$\dot{I}_B^* < 0$$

$$\frac{dI_B}{dt} = \frac{1}{L_2}V_B - \frac{R_2}{L_2}I_B - \frac{u_3}{L_2}V_o \tag{9}$$

Then, combining the dynamic equations yields the dynamic model of the battery's operation as follows:

$$u_{23} = \begin{cases} 1-u_2 & i_B^* > 0 \\ u_3 & i_B^* < 0 \end{cases}$$

$$\frac{dI_B}{dt} = \frac{V_B}{L_2} - \frac{R_2 I_B}{L_2} - \frac{u_{23}V_o}{L_2} \tag{10}$$

$$I_2 = u_3 I_B \tag{11}$$

$$I_o = I_1 + I_2 = (1-u_1)I_{pv} + u_3 I_B \tag{12}$$

$$\frac{dV_o}{dt} = \frac{1-u_1}{C}I_{pv} + \frac{u_{23}}{C}I_B - \frac{1}{C}I_o \tag{13}$$

2.4 Sliding Mode Control Strategy

The sliding mode theory is a highly well-suited application for DC-DC converters since they are inherently changeable structure systems whose topology changes while operating. The SMC is one of the well-known nonlinear control methods. It defines the sliding surface according to the system's control goals, which are associated with the errors between the measured and reference variables since the control scheme pursues to lessen the error to zero, in contrast to a standard PI controller, which has relatively weak stability and robustness against load disturbances, variations in the converter input voltage, and parameter uncertainties. The SMC offers distinct benefits for the control of converters, including stability against extreme variations in load and parameter uncertainty, excellent robustness, and quick dynamic response. Three stages are necessary to properly design the SMC: choosing a sliding surface, creating the control law, and ensuring the controller's stability. The SMC forces the trajectories of the system to reach an assumed surface called the sliding surface and stays on it; thereby, the system is in sliding mode, as shown in Figure 8.

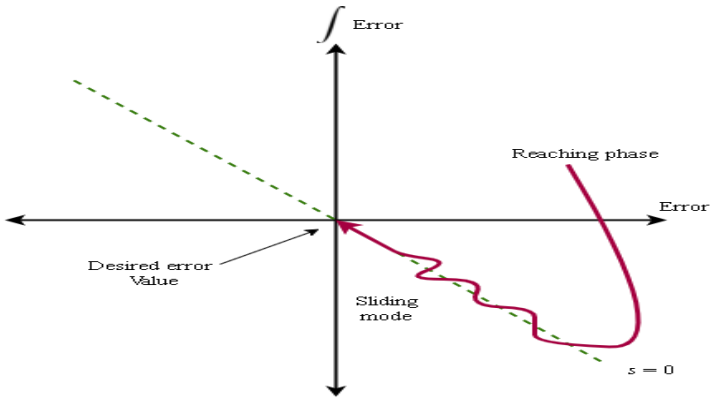

Figure 8. Graphical interpretation of SMC.

Therefore, the sliding surfaces of SMCs in both PV and ESS systems are assumed to be:

$$s_1 = e_1(t) + \lambda_{11} \int e_1(t)dt \tag{14}$$

$$s_2 = e_2(t) + \lambda_{22} \int e_2(t)dt \tag{15}$$

Here, λ_{11} and λ_{22} are positive design constants, and the tracking error variables e_1 and e_2 are also assumed to be

$$e_1 = I_{pv} - I_{pv}^* \tag{16}$$

$$e_2 = I_B - I_B^* \tag{17}$$

Where I_{pv}^* represents the reference current generated by the MPPT method. Therefore, the sliding surfaces become

$$s_1 = (I_{pv} - I_{pv}^*) + \lambda_{11} \int (I_{pv} - I_{pv}^*)dt \tag{18}$$

$$s_2 = (I_B - I_B^*) + \lambda_{22} \int (I_B - I_B^*)dt \tag{19}$$

The control law's principal goals are to keep the system's trajectory on the sliding surface and to enforce the selected dynamic. The chosen control laws are configured utilizing the principle of the equivalent and nonlinear control of u_{eq1} and u_{n1}, u_{eq23} and u_{n23} for PV and ESS systems, respectively. Therefore, the control laws are as follows:

$$u_1(t) = u_{eq1} + u_{n1} \tag{20}$$

$$u_{23}(t) = u_{eq23} + u_{n23} \tag{21}$$

The nonlinear components u_{n1} and u_{n23} are called switching controls which are employed to keep the system's dynamics on the sliding surface, and they can be rewritten as u_{sw1} and u_{sw23}.

The equivalent component for Equations (20) and (21) are derived by considering that the time derivative of sliding surfaces which described by:

$$\dot{s}_1(x) = \dot{s}_2(x) = 0 \tag{22}$$

Therefore, the equivalent control u_{eq1} can be found as follows:

$$\dot{s}_1(x) = 0$$
$$\left(\frac{dI_{pv}}{dt} - \frac{dI_{pv}^*}{dt}\right) + \lambda_{11}\left(I_{pv} - I_{pv}^*\right) = 0 \tag{23}$$

$$\left(\frac{V_{pv}}{L_1}-\frac{R_1 I_{pv}}{L_1}-\frac{V_o}{L_1}\left(u_{eq1}-1\right)-\frac{dI_{pv}^*}{dt}\right)+\lambda_{11}\left(I_{pv}-I_{pv}^*\right)=0$$

$$\frac{V_o}{L_1}\left(u_{eq1}-1\right)=\frac{V_{pv}}{L_1}-\frac{R_1 I_{pv}}{L_1}+\lambda_{11}\left(I_{pv}-I_{pv}^*\right)-\frac{dI_{pv}^*}{dt}$$

$$u_{eq1}=\frac{V_{pv}+(\lambda_{11}L_1-R_1)I_{pv}-L_1(\frac{dI_{pv}^*}{dt}+\lambda_{11}I_{pv}^*)}{V_o}+1$$

Also, the equivalent control u_{eq23} can be found as follows:

$$\begin{gathered}\dot{s}_2(x)=0\\ \left(\frac{dI_B}{dt}-\frac{dI_B^*}{dt}\right)+\lambda_{22}(I_B-I_B^*)=0\\ \left(\frac{V_B}{L_2}-\frac{R_2 I_B}{L_2}-\frac{u_{eq23}V_o}{L_2}-\frac{dI_B^*}{dt}\right)+\lambda_{22}(I_B-I_B^*)=0\\ \frac{V_o}{L_2}u_{eq23}=\frac{V_B}{L_2}-\frac{R_2 I_B}{L_2}-\frac{dI_B^*}{dt}+\lambda_{22}(I_B-I_B^*)\\ u_{eq23}=\frac{V_B+(\lambda_{22}L_2-R_2)I_B-L_2(\frac{dI_B^*}{dt}+\lambda_{22}I_B^*)}{V_o}\end{gathered} \tag{24}$$

The main merit of the higher-order SMC is that the conventional SMC's chattering noise can be eliminated. The super twisting controller has two terms, the first of which is a continuous function of the derivative of the sliding variable. In contrast, the second is a discontinuous function of the sliding variable. It can be addressed by [45]

$$\begin{gathered}w(t)=-\lambda_a|s|^p sgn(s)+v\\ \dot{v}(t)=-\lambda_b sgn(s)\end{gathered} \tag{25}$$

Moreover, the super-twisting algorithm's merits are the simplicity of development, negligible chattering, and robustness against uncertainties. Therefore, an adaptive sliding mode control based on the super-twisting algorithm is developed to enhance the convergence time to the sliding surface and prevent chattering issues. The super-twisting sliding mode control aims to create appropriate control laws for the STSMCs in PV and ESS systems under model uncertainties and external disturbances. Therefore, each system's control law combines an equivalent that drives the system to reach the sliding surface using Equations (23)-(24) and switching control that attains robustness to disturbances and uncertainties, lessens chattering, and pushes the dynamics of the system into the sliding surface. Following is how the control law for each system is built using the super twisting method:

$$\begin{gathered}u_{sw1}(t)=-\lambda_{a_1}|s_1|^p sgn(s_1)-\lambda_{b_1}\int sgn(s_1)dt\\ u_{sw23}(t)=-\lambda_{a_{23}}|s_2|^p sgn(s_2)-\lambda_{b_{23}}\int sgn(s_2)dt\end{gathered} \tag{26}$$

Thus, the control laws for PV and ESS systems are as follows:

$$\begin{gathered}u_1(t)=u_{eq1}+u_{sw1}\\ u_{23}(t)=u_{eq23}+u_{sw23}\end{gathered} \tag{27}$$

Therefore, the control law for STSMC in the PV system becomes

$$u_1(t) = \frac{V_{pv} + (\lambda_{11}L_1 - R_1)I_{pv} - L_1(\frac{dI_{pv}^*}{dt} + \lambda_{11}I_{pv}^*)}{V_o} + 1 - \lambda_{a_1}|s_1|^p sgn(s_1) - \lambda_{b_1}\int sgn(s_1)dt \quad (28)$$

Also, for STSMC in the ESS system, the control law becomes

$$u_{23}(t) = \frac{V_B + (\lambda_{22}L_2 - R_2)I_B - L_2(\frac{dI_B^*}{dt} + \lambda_{22}I_B^*)}{V_o} - \lambda_{a_{23}}|s_2|^p sgn(s_2) - \lambda_{b_{23}}\int sgn(s_2)dt \quad (29)$$

Here, λ_{11}, λ_{a1} , $\lambda_{b1,}$ and λ_{22}, λ_{a23} , λ_{b23} are positive gains; $0 < \rho \leq 0.5$ is a fractional coefficient [46].

From (25), after assuming that the disturbance *d* is bounded, such as $|d \leq \delta|$ where δ is a known positive constant, the closed loop system can be given as

$$\dot{w}(t) = -\lambda_a|s|^p sgn(s) + v + d \quad (30)$$
$$\dot{v}(t) = -\lambda_b sgn(s)$$

Therefore, to demonstrate the stability of STSMC in a PV system, the Lyapunov function is selected as follows [47]

$$V = 2b_1|s_1| + \frac{1}{2}v^2 + \frac{1}{2}(a_1|s_1|^{0.5}sign(s_1) - v)^2 \quad (31)$$

$$V = \zeta^T P\zeta \quad (32)$$

Here,

$\zeta^T = [|s_1|^{0.5}sign(s_1)v]$

$P = \frac{1}{2}\begin{bmatrix} 4b_1 + a_1^2 & -a_1 \\ -a_1 & 2 \end{bmatrix}$

The time derivative of the Lyapunov function, as well as the solution of Equation (30), can result as follows:

$$\frac{dV}{dt} = -\frac{1}{|s_1|^{0.5}}\zeta^T Q\zeta + \frac{1}{|s_1|^{0.5}}q^T\zeta \quad (33)$$

Here,

$q^T = [(2b_1 + \frac{a_1^2}{2}) \quad -\frac{a_1}{2}]$

$Q = \frac{a_1}{2}\begin{bmatrix} 4b_1 + {a_1}^2 & -a_1 \\ -a_1 & 1 \end{bmatrix}$

Applying the bounds for the disturbance *d*, as indicated in [48] , It is possible to reduce the derivative Lyapunov function to

$$\frac{dV}{dt} = -\frac{1}{|s_1|^{0.5}}\zeta^T\hat{Q}\zeta \quad (34)$$

Here,

$$\hat{Q} = \frac{a_1}{2}\begin{bmatrix} 4b_1 + a_1^2 - (\frac{4b_1}{a_1} + a_1)\delta & -(a_1 + 2\delta) \\ -(a_1 + 2\delta) & 1 \end{bmatrix}$$

Therefore, if $\dot{V} < 0$ if $\hat{Q} > 0$, this proves that the system is asymptotically stable if the gains parameters fulfill

$$\begin{cases} a_1 > 2\delta \\ b_1 > a_1 \dfrac{5a_1\delta + 4\delta^2}{2(a_1 - 2\delta)} \end{cases} \tag{35}$$

Also, for STSMC in the storage system, if $\dot{V} < 0$ if $\hat{Q} > 0$,with changing a_1 to a_2, b_1 to b_2, and s_1 to s_2, the system is asymptotically stable if the gains parameters also fulfill

$$\begin{cases} a_2 > 2\delta \\ b_2 > a_2 \dfrac{5a_2\delta + 4\delta^2}{2(a_2 - 2\delta)} \end{cases} \tag{36}$$

It should be mentioned that the gain parameters (λ_{11}, λ_{a1} , $\lambda_{b1,}$ λ_{22}, λ_{a23} , λ_{b23}) for both boost and buck-boost converters are tuned using CSA and GWO methods.

2.5 Energy Storage System

The on-grid ESS, as depicted in Figure 1, is connected to a DC link and has an 800 Ah capacity (5 lithium-ion batteries, each with a nominal 24 V and 160 Ah), a nominal 120 V, and a 50% state of charge (its data are provided in Table A3) [49]. The proposed ESS system is utilized to smooth out fluctuations in the PV system's production due to the unpredictable nature of solar irradiance levels. The ESS uses a bi-directional buck-boost converter to charge the battery or discharge its batteries to the system according to the energy fluctuations in the PV system's output. For this lithium-ion battery type, the model uses the following equations [50]:

- Discharge model ($i^* > 0$)

$$f_1(it, i^*, i) = E_0 - \frac{KQ}{Q - it}(i^* - it) + Ae^{-B \times it} \tag{37}$$

- Charge model ($i^* < 0$)

$$f_2(it, i^*, i) = E_0 - \frac{KQi^*}{it + 0.1Q} - \frac{KQ}{Q - it} \times it + Ae^{-B \times it} \tag{38}$$

Here, f_1 and f_2 are the battery voltage (V) for discharge and charge states, respectively, E_0 is the constant voltage (V), K is the polarization constant (V/Ah), i^* is the low-frequency current dynamics (A), i is the battery current (A), it is the extracted capacity (Ah), Q is the maximum battery capacity (Ah), A is the exponential voltage (V) and B is the exponential capacity (Ah^{-1}).

2.6 DC-AC Inverter control

The voltage source inverter (VSI) is linked to the primary grid via an LC filter, as displayed in Figure 9. The VSI control mode significantly impacts how well inverter-based PV systems function. Therefore, a PQ controller is required for the inverter control. In VSI control, voltage and frequency are regulated concerning their reference parameters using the PQ controller, which modifies the inverter current's amplitude and phase angle to force the VSI to supply a specific amount of apparent power into the primary grid.

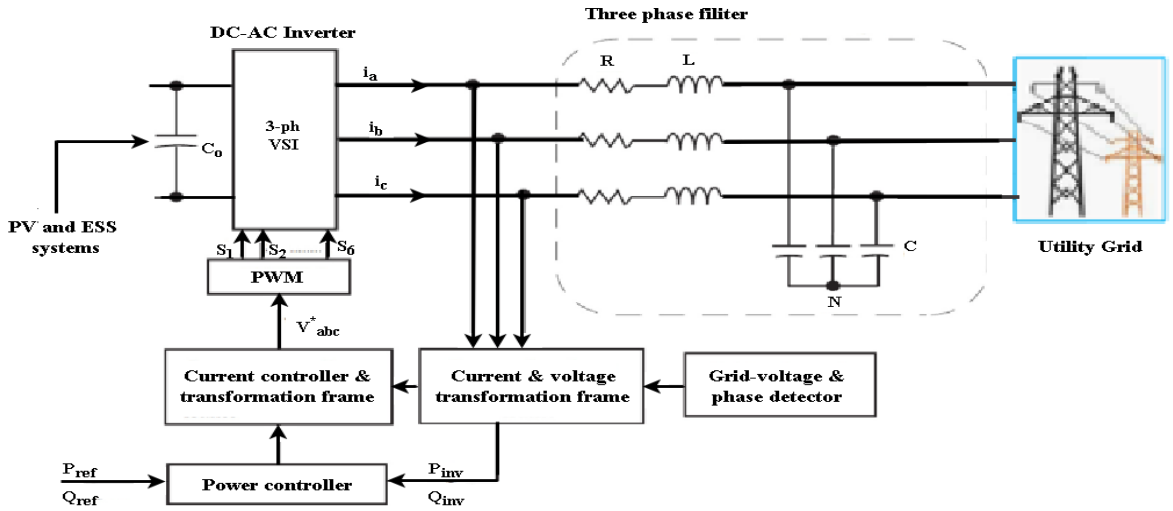

Figure 9. DC-AC Inverter controller

3. Methodology

The introduced maximum power tracking method, CSA, is interconnecting the PV power source and the DC link, which allows the PV modules to operate at MPP regardless of the operating conditions. Moreover, CSA is made up with a switch-mode DC boost converter whose duty cycles are modified to draw the right amount of current and therefore maximizes the PV modules' efficiency. Also, the CSA is integrated with STSMC that used to regulate the PV voltage with a reference generated by MPPT and minimizes the error between these voltages or currents in the ESS as small as possible. However, the gain parameters of STSMCs need to be tuned for better performance. Therefore, the CSA is also used to find the optimal values of STSMC's gains in PV and storage systems based on the integral of time multiplied by absolute error (ITAE) criteria, which is provided by Equation (39) [51].

$$Min \text{ ITAE} = \int_0^t t\,|e(t)|\,dt \tag{39}$$

Here, $e(t)$ is the error between a measured signal (voltage/current) and a reference signal in PV and ESS systems.

The CSA pursues the MPP in the PV modules based on the objective function in Equation (40).

$$Max\ \ P_{pv} = V_{pv} \times I_{pv} \tag{40}$$

Here, I_{pv} is the drawn current from a PV cell, and V_{pv} is its corresponding output voltage.

The CSA is a recent metaheuristic optimization algorithm that proposed by M. Qais et al. [52], and is motivated by the geometrical characteristics of circles. The geometric circle is a primary closed curve with a constant distance between each point and the center. The circle's circumference is the length of the curve that surrounds it, and its diameter is calculated by connecting two points on the curve that cross at its center (x_c) and the circle's radius (R) is the distance from any point on it to x_c as illustrated in Figure 10. It is also obvious that the tangent line segment is a straight line perpendicularly intersects the radius R. Pythagorean equations define the right triangle's orthogonal function (Tan) as the ratio of the circle's radius to the perpendicular tangent line segment in which the tangent line

segment is the distance between the two points x_t and x_p. The orthogonal function is represented by the following Equation:

$$Tan(\theta) = \frac{x_t - x_c}{x_p - x_t} \tag{41}$$

Then,

$$x_t = x_c + (x_p - x_t) \times Tan(\theta) \tag{42}$$

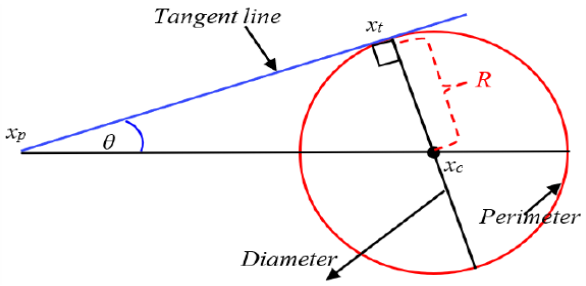

Figure 10. Terminology for the circle in geometry.

The CSA searches inside random circles to enlarge the search region for the best solution. Utilizing the circle's center as a reference point, the angle (θ) between the tangent line's contacting point and the circle's circumference gradually reduces as it approaches the circle's center, as demonstrated in Figure 11a. Since there's a chance that this circle can be stuck in a local minimum/maximum solution, as seen in Figure 11b, the angle where the tangent line touches the point is randomly reformed. The center point x_c is regarded as the optimal position in the algorithm, and the touching point x_t is considered as the CSA's search agent. As depicted in Figure 11, the CSA modifies its search agent as a result of the movement of the touching point x_t to the center point x_c. To avoid trapping the CSA in a local minimum/maximum solution, the touching point will be randomly altered by modifying the angle θ. A flowchart explained the phases of CSA method is depicted Figure 12.

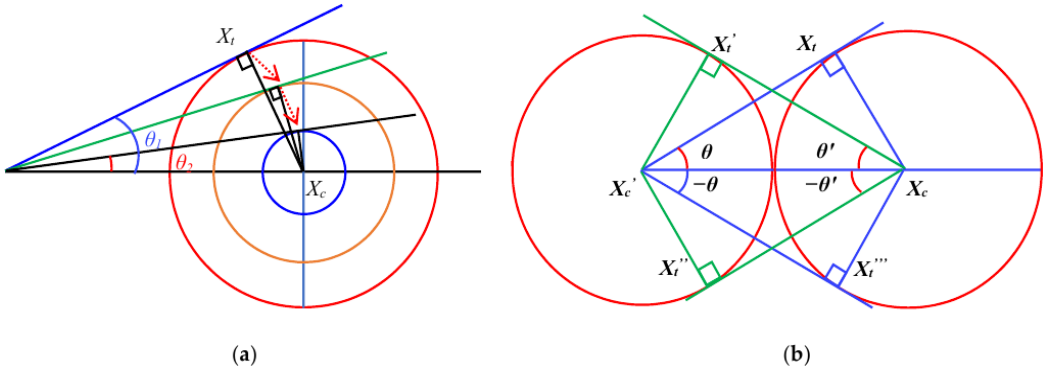

Figure 11. The procedures of the CSA method (a) exploitation (b) exploration.

The introduced CSA method's major phases are explained as follows:

Phase 1: Initialization: This phase is crucial in the CSA because it allows equally randomizing all the search agent's dimensions. Afterward, as shown in Equation (43), the CSA's search agents are initiated between the search space's upper (*ub*) and lower (*lb*) limits.

$$x_t = up + r \times (ub - lb) \tag{43}$$

Here, *r* is a random vector range from 0 to 1.

Phase 2: I *Update the search agent position:* the search agent x_t position, in this phase, is updated in accordance with the estimated best position x_c as illustrated in Equation (44).

$$x_t = x_c + (x_c - x_t) \times Tan(\theta) \tag{44}$$

Here, the angle θ, which is a crucial component of exploring and exploiting the CSA, can be computed as follows:

$$\theta = \begin{cases} w \times rand & if\ iter > c \\ w \times p & otherwise \end{cases} \tag{45}$$

Here,

$$w = a \times rand - a \tag{46}$$

$$a = \pi - \pi \times (\frac{iter}{maxiter})^2 \tag{47}$$

$$p = 1 - 0.9\sqrt{\frac{iter}{maxiter}} \tag{48}$$

Here, *c* is a constant in the range of 0 and 1, which specifies the maximum iterations' percentage, *Maxiter* stands for the maximum number of iterations, *iter* is an iteration counter, and *rand* is a random value between 0 and 1. Equation (46) demonstrates how the *w* value varies from π to 0 as *iter* increases. Also, Equation (47) states that the variable *a* varies from *pi* to 0. And, the variable *p* ranges from 1 to 0, as illustrated in Equation (48). Therefore, the angle θ ranges from *pi* to 0 as well.

The CSA can be successful in the following two scenarios:

Scenario 1: iter > (c × Maxiter): for all the time, this scenario means that the angle $\theta = w \times rand$, which used to boost the CSA's exploration process and skip the local minima.

Scenario 2: *i*ter < (c × Maxiter): for all the time, this scenario sets the angle $\theta = w \times p$, which is employed to improve the CSA's exploitation process.

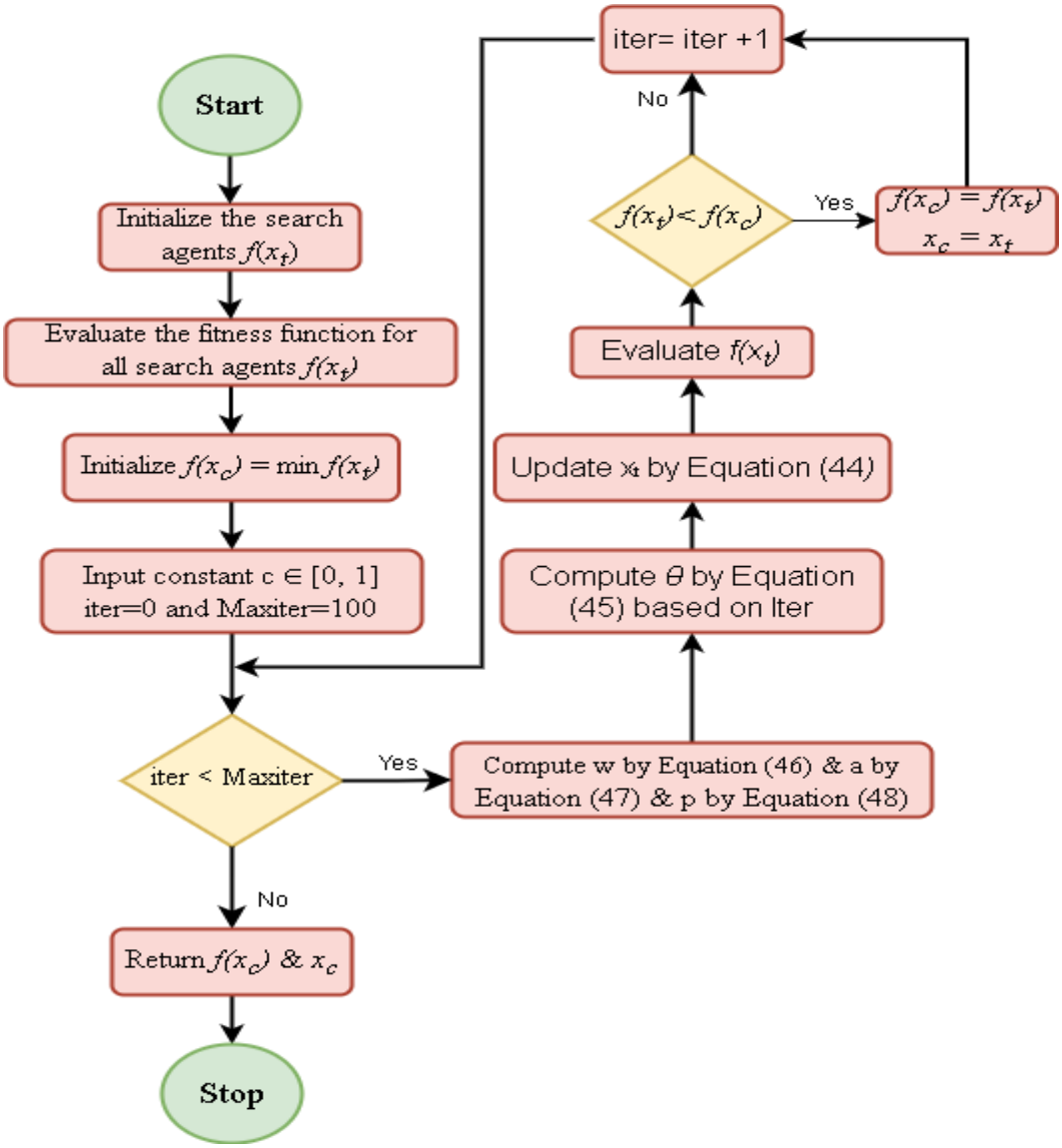

Figure 12. Flowchart of the CSA method.

4. Results and Discussions

MATLAB/Simulink software [53] is utilized to optimize and simulate the proposed systems. In the optimization stage, the STSMC and PI controllers were tuned using the CSA and GWO methods (Table 1 explains the parameters of these two methods). Then, the proposed systems' performance was evaluated using CSA-STSMC, CSA-PI, and GWO-STSMC for the MPP tracking of 100 kW of five different commercial PV modules.

Table 1. Parameters of the proposed methods.

Parameter	Method	
	CSA	GWO
No. of particles/populations	30	30

No. of iterations	100	100
Dimension (No. of variables)	6	6
Constant c	[0,1]	---
Random number *rand*	[0,1]	---
Random vectors $r_1 and\ r_2$	[0,1]	[0,1]
coefficient vector $\vec{v}$	---	[0,2]

4.1 Optimization Results

Figure 7 shows that a PV system consisting of commercial ASi-PV modules with a capacity of 100kW gives more power than other commercial modules under non-standard test conditions. Therefore, the ASi-PV system was used for optimization purposes. The introduced CSA and GWO methods were utilized to identify the optimal values of STSMC and PI controllers' gains using the objective function based on ITAE criteria in Equation (39) which is the summation of the errors $e_{pv}(t)=(V_{pv}-V_{MPPT_{ref}})$ and $e_{ESS}(t)=\left(I_{bat}-I_{charge_{ref}}\right)+(I_{bat}-I_{discharge_{ref}})$ of PV and ESS systems, respectively. In this work, the proposed STSMC or PI controllers were used to regulate the measured signals (voltage or current) with respect to reference ones in PV and storage systems. Table 2 shows that using CSA-STSMC, the gains λ_{11}, λ_{a1} and λ_{b1} are 88.47, 101.62 and 138.79, respectively for the STSMC in the PV system. While the gains of STSMC in the ESS λ_{22}, λ_{a23} and λ_{b23} are 176.62, 38.43 and 61.83, respectively. These gains for both systems converge the ITAE value to the best minimum, which is 0.89, compared to the values 0.93 and 0.90 using CSA-PI and GWO-STSMC methods, respectively. Figure 13 shows the convergence curves of optimal gains for STSMC and PI controllers using CSA-STSMC, CSA-PI, and GWO-STSMC methods.

Table 2. Optimization results for optimal controllers' gains by CSA-STSMC, CSA-PI, and GWO-STSMC methods.

Method	**System**	**Gain value**		**Optimal ITAE**
CSA-STSMC	PV	λ_{11}	88.47	0.89
		λ_{a1}	101.62	
		λ_{b1}	138.79	
	ESS	λ_{22}	176.62	
		λ_{a23}	38.43	

		λ_{b23}	61.83	
CSA-PI	PV	k_{p1}	2.88	0.93
		k_{i1}	200	
	ESS	k_{p2}	54.80	
		k_{i2}	1.18	
		k_{p3}	14.29	
		k_{i3}	53	
GWO-STSMC	PV	λ_{11}	106.25	0.90
		λ_{a1}	114.31	
		λ_{b1}	145.69	
	ESS	λ_{22}	193.11	
		λ_{a23}	142.56	
		λ_{b23}	182.76	

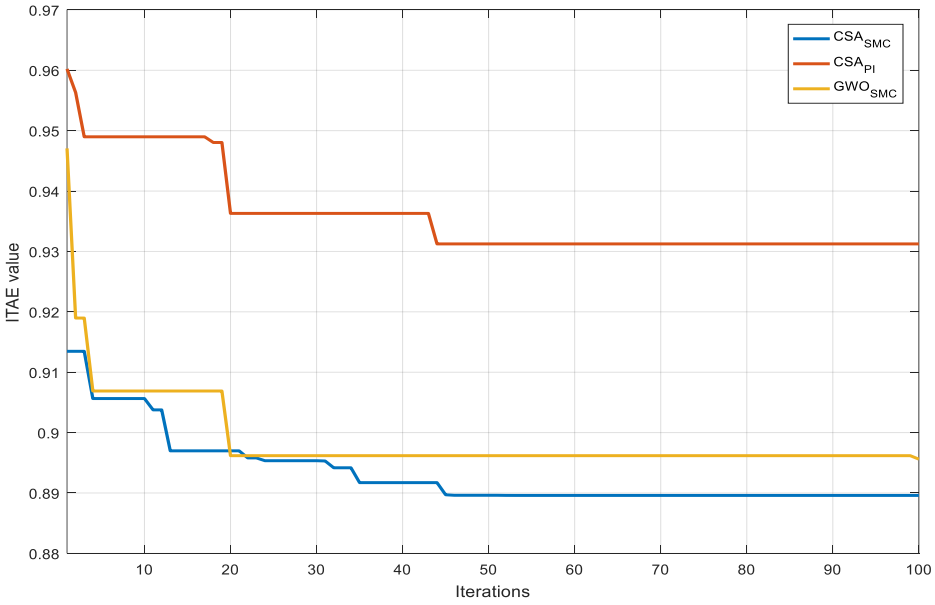

Figure 13. Convergence curves of optimal gains for STSMC and PI controllers using CSA-STSMC, CSA-PI, and GWO-STSMC methods.

4.2 Simulation Results

The performance of the proposed 100 kW systems of five different commercial PV modules (ASi, CdTe, CIS, McSi, and PcSi) is simulated using the CSA-STSMC method for tracking their MPP at non-standard operation conditions

shown in Figures 4 and 5. Moreover, CSA-PI and GWO-STSMC methods have been used to compare the proposed method's effectiveness. Figures 14a-14e show the reference voltages generated by the introduced MPPT methods compared to PV voltage for all different PV modules. Also, it can be seen that the PV and reference voltages are zeros when the irradiance level is zero (during the night). Afterward, they increase until the maximum power is attained at this specific value of irradiance level. They follow the irradiance level up and down, especially at 9 AM and between 2 and 3 PM when the partial shading conditions occur. Furthermore, the PV and reference's voltages vary between 268-310V, 290-315 V, 265-298 V, 274-298 V, and 275-298 V for ASi, CdTe, CIS, McSi, and PcSi modules, respectively. Also, the boost converter's output voltage varies between 499 and 501 V for all different PV modules, as displayed in Figures 15a-15e.

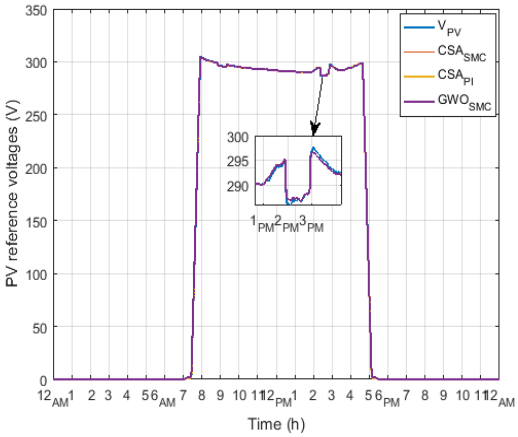

(a) ASi Modules

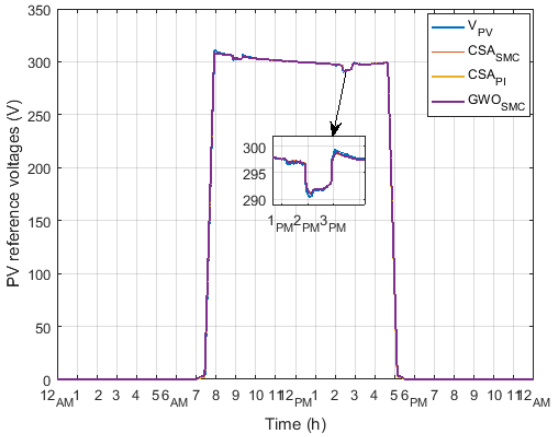

(b) CdTe Modules

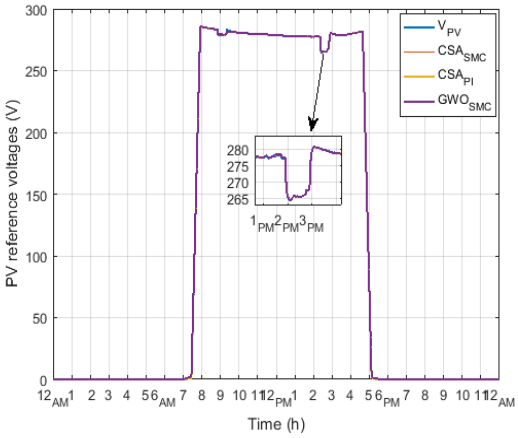

(c) CIS Modules

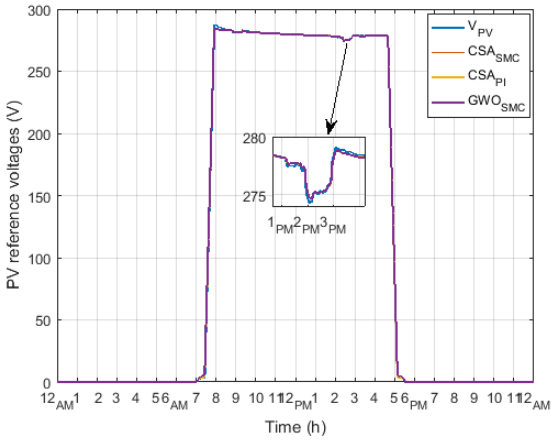

(d) McSi Modules

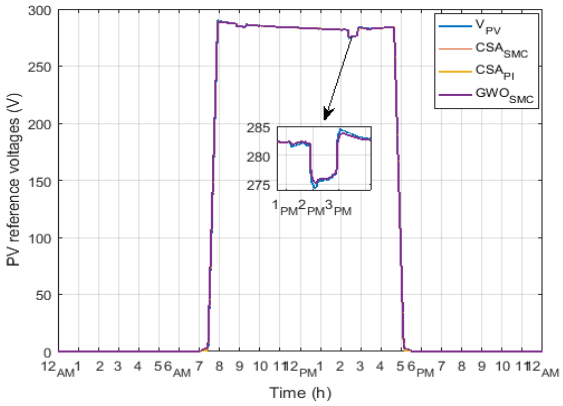

(e) PcSi Modules

Figure 14. PV voltage compared to reference voltages (V) using CSA-STSMC, CSA-PI, and GWO-STSMC methods of different PV modules.

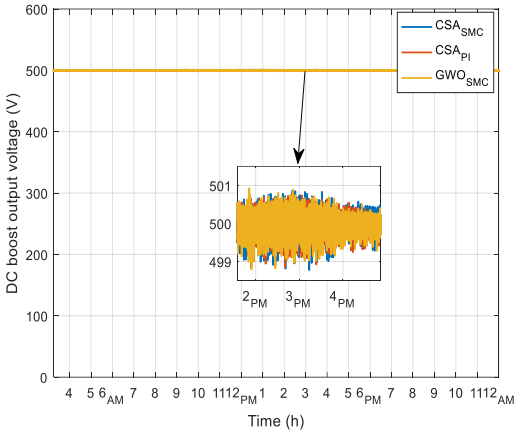

(a) ASi Modules

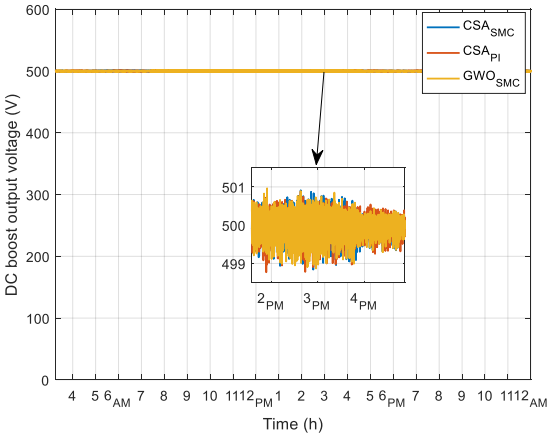

(b) CdTe Modules

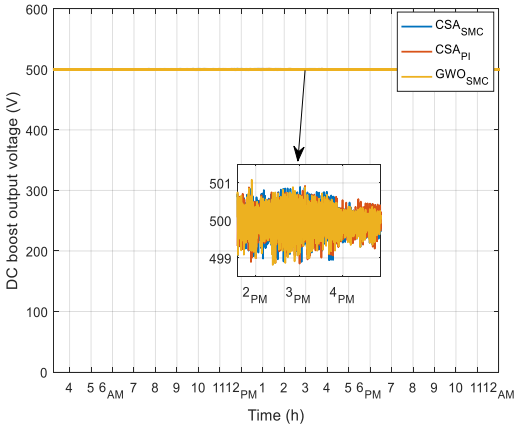

(c) CIS Modules

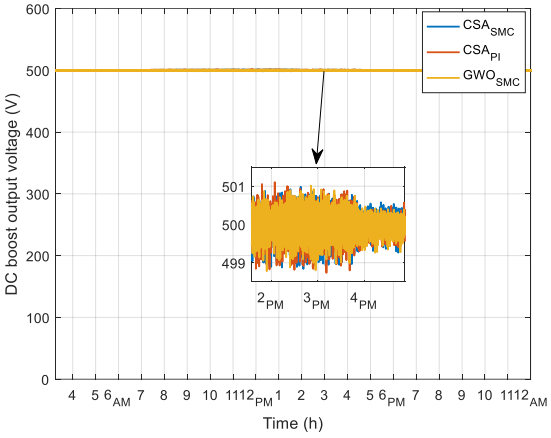

(d) McSi Modules

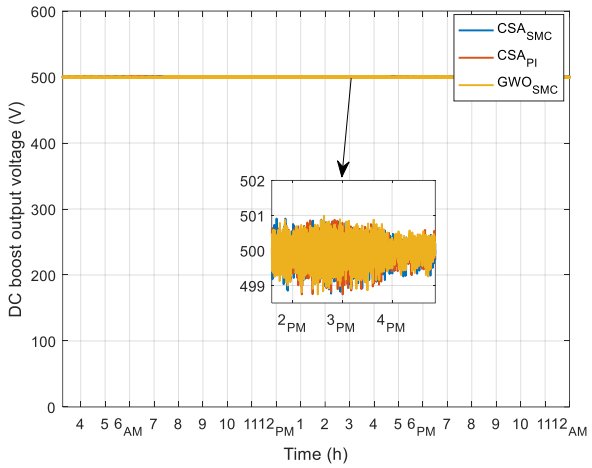

(e) PcSi Modules

Figure 15. DC to DC boost output voltages (V) using CSA-STSMC, CSA-PI, and GWO-STSMC methods of different PV modules.

Figure 16 illustrates the corresponding output power of different PV modules. As can be found that the PV's produced power follows solar irradiance level either increasing or decreasing. As shown in Figures 16a-16e, the proposed method (CSA-STSMC) can extract more power than CSA-PI and GWO-STSMC methods. Thus, for ASi, CdTe, CIS, McSi and PcSi-PV systems, respectively, the extracted powers are 101.91-, 101.85-,101.82-kW and 101.10-, 100.60-, 100.67-kW and 100-, 99.90, 99.88-kW and 101.53-, 101.26- 101.30-kW and 101.32-, 101-, 100.91-kW using CSA-STSMC, CSA-PI and GWO-STSMC methods, respectively. Therefore, the improvements in extracting power using the proposed method compared to other methods are 0.10%,0.50%,0.12%,0.27%, and 0.40% for ASi, CdTe, CIS, McSi, and PcSi-PV systems, respectively.

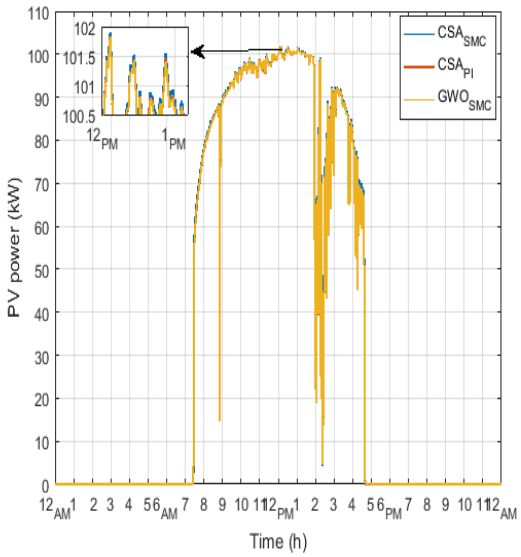

(a) ASi Modules

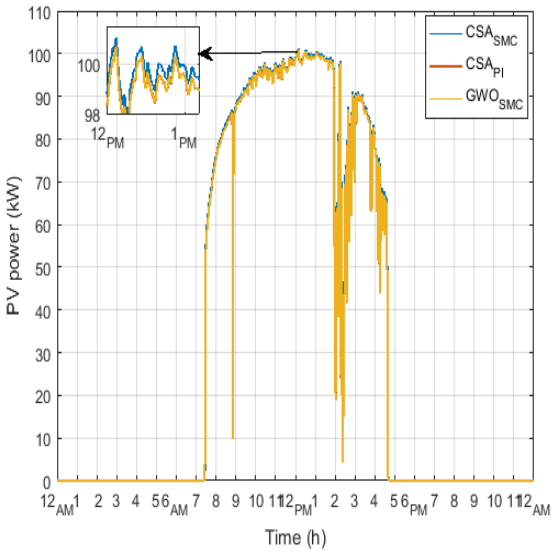

(b) CdTe Modules

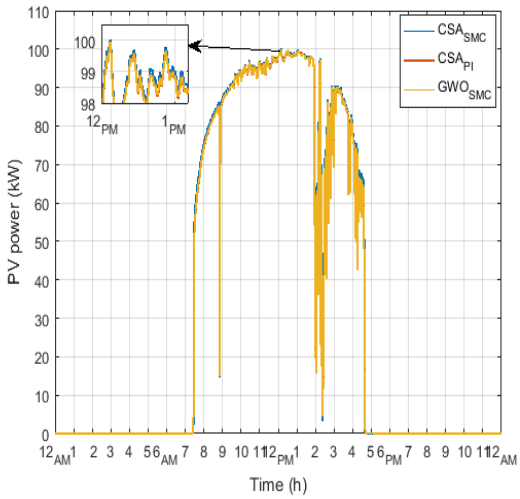

(c) CIS Modules

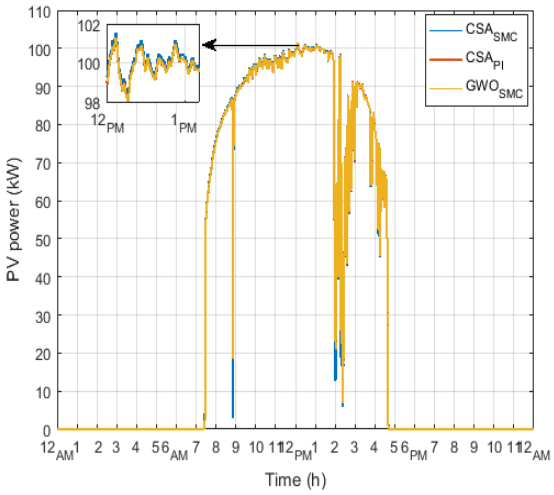

(d) McSi Modules

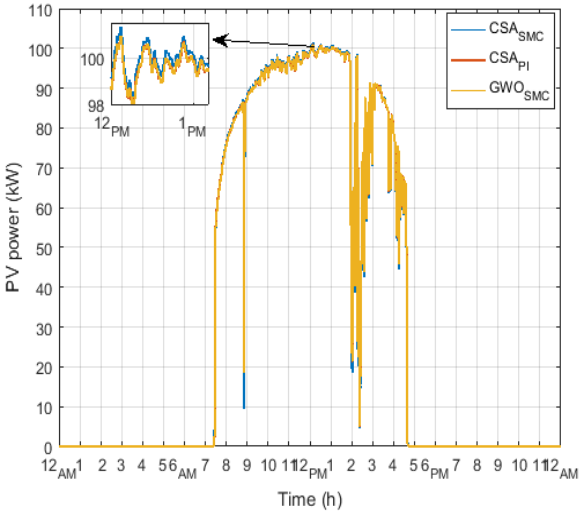

(e) PcSi Modules

Figure 16. PV power (kW) using CSA-STSMC, CSA-PI, and GWO-STSMC methods of different PV modules.

Also, Figure 17 demonstrates ESS's corresponding charging and discharging currents for smoothing the output power fluctuations of PV systems. The currents follow these fluctuations to make the utility grid receive a 100 kW regardless of irradiance level. As displayed in Figures 17a-17e, the ESS discharges its power with 792 A during the night when the PV systems are out till 7:15 AM, and then the discharging currents decrease according to the PV systems' output power till they reach zero. Afterward, the ESS system starts charging its batteries between 12 and 2 PM because, at this time, PV systems produce power of more than 100 kW. Moreover, between 12 and 2 PM, the charging currents using CSA-STSMC, CSA-PI, and GWO-STSMC methods, respectively, for ASi, CdTe, McSi, and PcSi-PV systems are 14.72, 14.32, 14 A (sign minus, in Figures 17a-17e, means charging) and 8.18, 4.75, 5.18 A and 11.87, 1.16, 10 A and 10.24, 7.79, 7.10 A, respectively. However, for the CIS-PV system, the produced power is less than 100 kW; thus, the ESS system discharges its power with 0.10, 0.80, and 0.88 A between 12 and 2 PM.

Furthermore, at this time, the charging power using CSA-STSMC, CSA-PI and GWO-STSMC methods, respectively, for ASi, CdTe, McSi and PcSi-PV systems are 1.90, 1.85, 1.81-kW and 1.10, 0.61, 0.67- kW and 1.53, 1.26, 1.30-kW and 1.32, 1, 0.91- kW, respectively. Also, for the CIS-PV system, the ESS system discharges its power with 0, 0.10, and 0.11 kW, as shown in Figures 18a-18e.

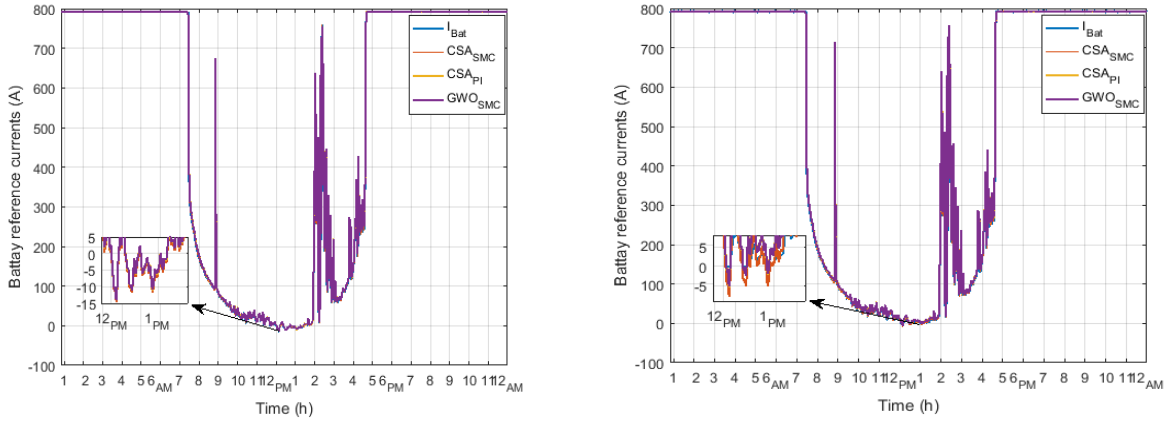

(a) ASi Modules (b) CdTe Modules

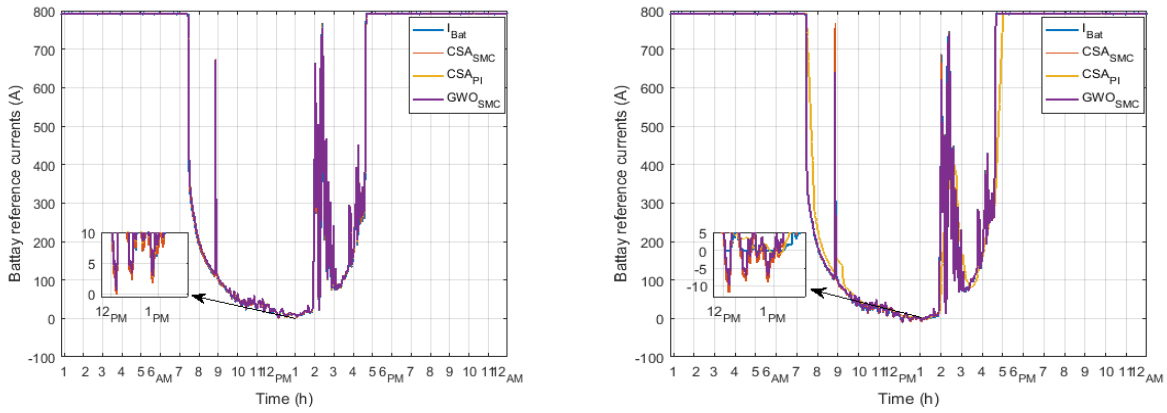

(c) CIS Modules (d) McSi Modules

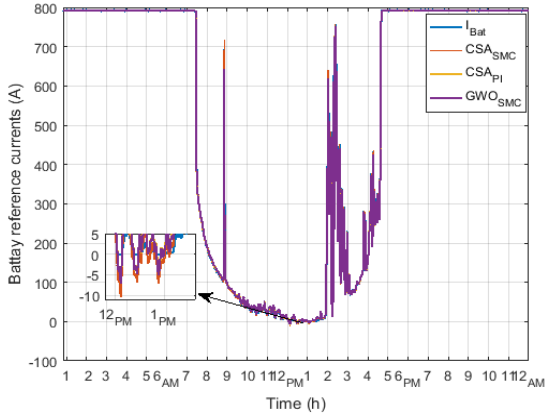

(e) PcSi Modules

Figure 17. Battery current as compared to reference currents (A) using CSA-STSMC, CSA-PI, and GWO-STSMC methods of different PV modules.

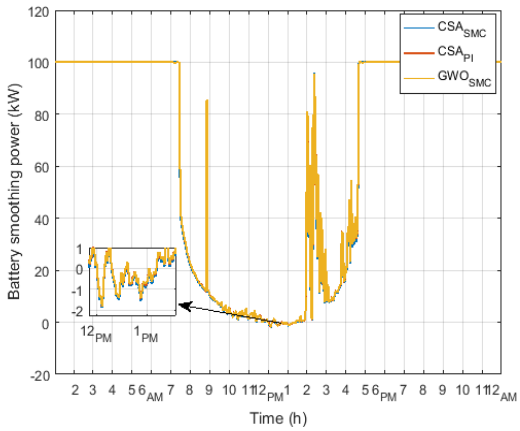

(a) ASi Modules

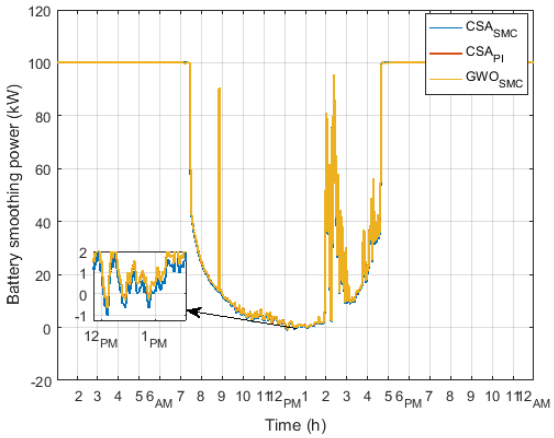

(b) CdTe Modules

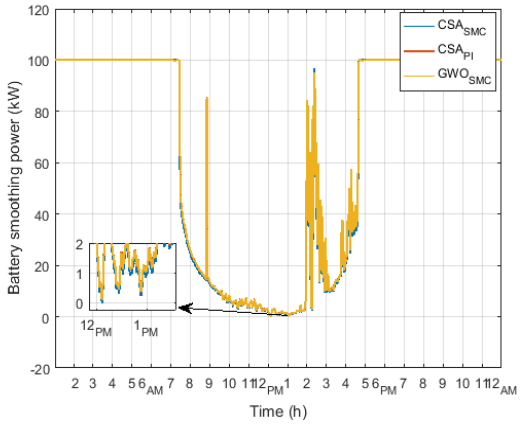

(c) CIS Modules

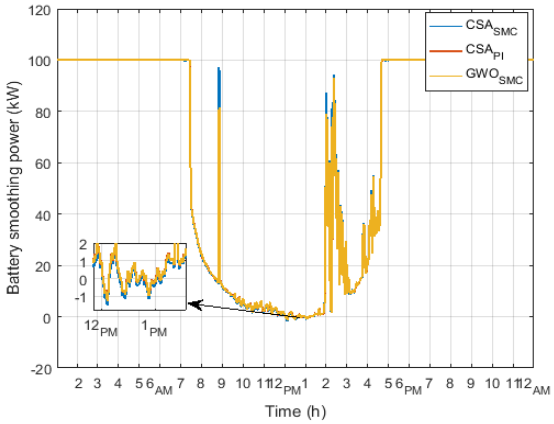

(d) McSi Modules

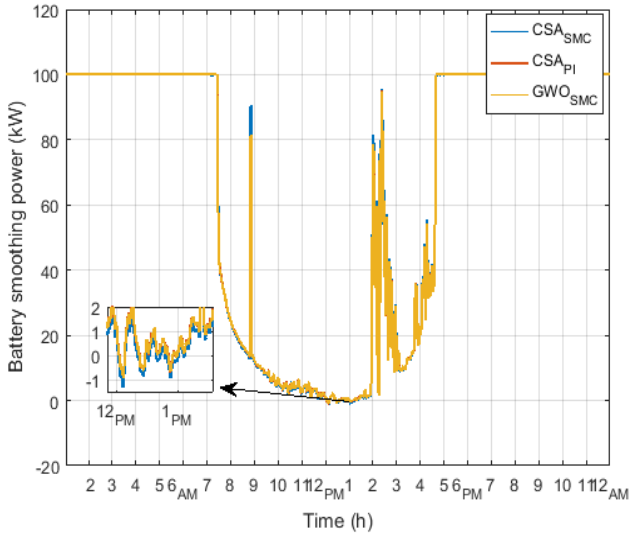

(e) PcSi Modules

Figure 18. Battery smoothing power (kW) using CSA-STSMC, CSA-PI, and GWO-STSMC methods of different PV modules.

Figure 19 demonstrates the AC loads converted from DC power of ASi, CdTe, CIS, McSi, and PcSi-PV systems using a three-phase inverter. As seen from Figures 19a-19e, the load is between 99.4 and 99.9 kW, where the power loss is less than 0.3 kW using CSA-STSMC, which is better than CSA-PI and GWO-STSMC methods. The corresponding three-phase currents and voltages for each of the ASi, CdTe, CIS, McSi, and PcSi-PV systems are shown in Figures 20 and 21.

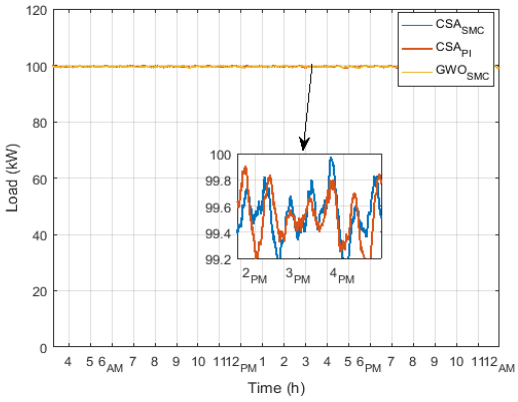

(a) ASi Modules

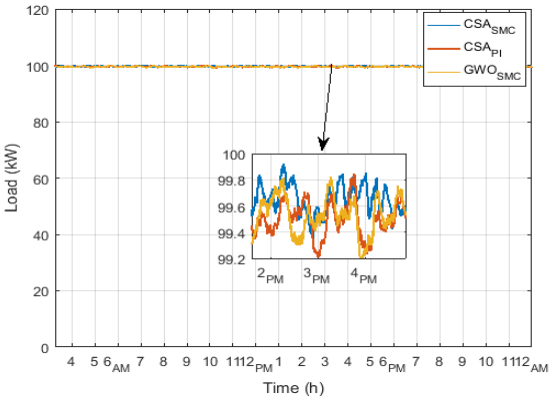

(b) CdTe Modules

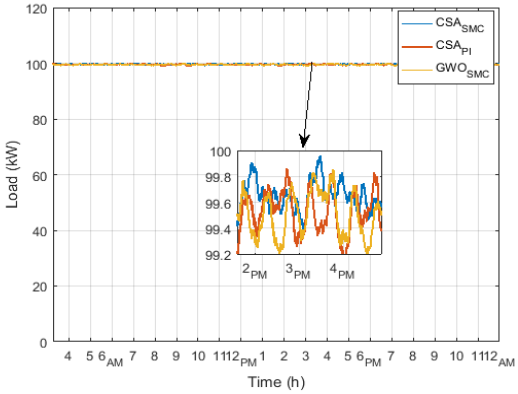

(c) CIS Modules

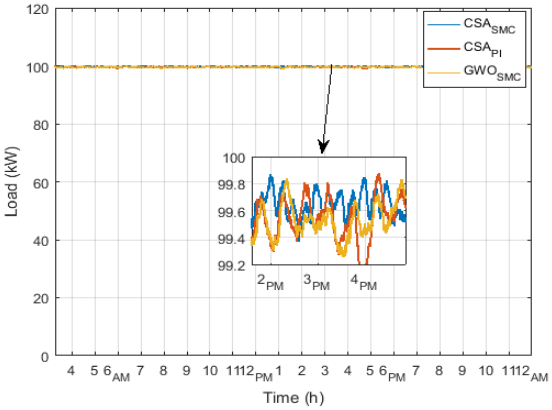

(d) McSi Modules

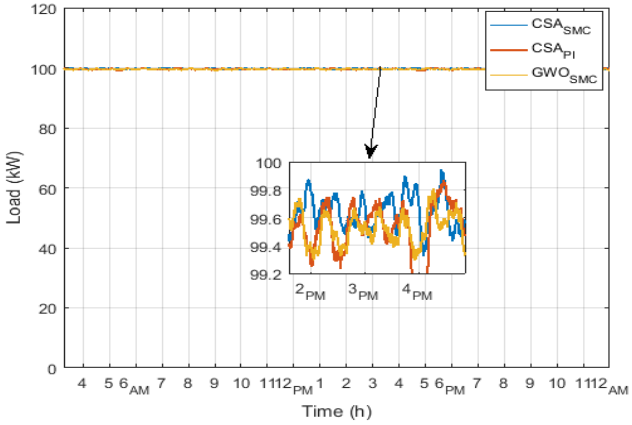

(e) PcSi Modules

Figure 19. Load (kW) using CSA-STSMC, CSA-PI, and GWO-STSMC methods of different PV modules.

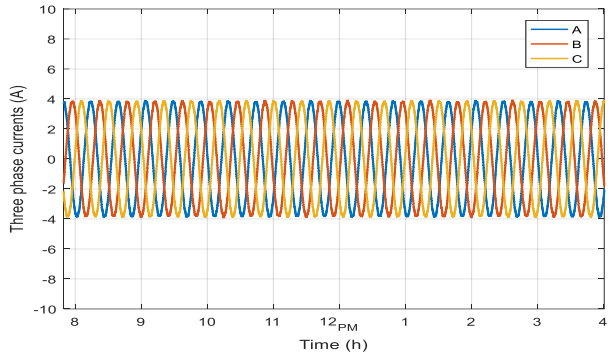

Figure 20. Three phase currents (A).

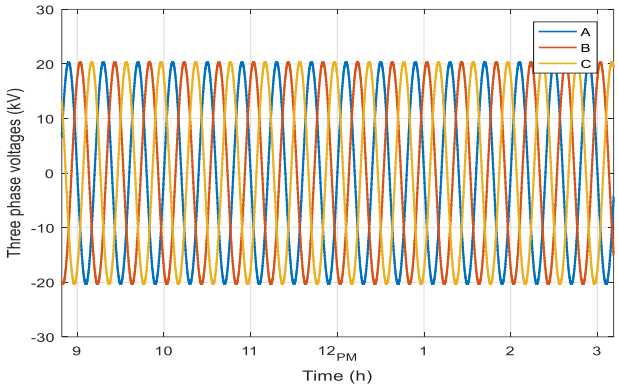

Figure 21. Three-phase voltages (kV).

To sum up, five different commercial PV systems have been evaluated in harsh weather conditions (using real data). The evaluation was done using the proposed method CSA integrated with STSMC for MPPT in the PV systems as well as another STSMC for optimal charging and discharging the ESS that is used to smooth any variations in the output of the PV systems. Furthermore, the performance of the proposed method was compared with CSA-PI and GWO-STSMC methods. Therefore, it can be seen from the aforementioned analysis that the proposed CSA method optimized the STSMC controller and converged to the best minimum value using the ITAE criteria and showed better tracking efficiency in maximizing the extraction power from such PV systems as compared to the considered methods.

5. Conclusions

This study has introduced a new application of the CSA to track the MPP of five commercial PV modules, ASi, CdTe, CIS, McSi, and PcSi. In addition, the STSMC controllers were used to regulate the PV voltage and battery current with respect to the corresponding references which provide better efficiency in maximizing the extracting power from the PV systems. Moreover, the performance of the CSA-STSMC method was compared with those of the CSA-PI and GWO-STSMC methods. Also, based on the P-V curves of PV modules, it can be seen that the commercial ASi-PV modules could produce more power than other modules under non-standard test conditions. Therefore, it was used for optimization purposes and the gain parameters of STSMC and PI controllers (in PV and ESSs) were tuned using CSA and GWO methods based on the ITAE criteria. Thus, the ITAE value was minimized towards the best minimum value, which is 0.89 using CSA-STSMC, compared with 0.93 and 0.90 using CSA-PI and GWO-STSMC methods, respectively. After tuning the introduced controllers, on the other hand, the proposed method was used to obtain the

MPP of 100-kW grid-connected systems and the ESS was used to smooth any power fluctuations in their output. Therefore, it was found that the improvements in the MPP's tracking using the proposed method compared with other methods are between 0.1% and 0.5% for the five commercial PV systems. Also, future studies shall concentrate on the expansion of this work from simulation studies to physical prototypes' implementation for different commercial PV modules.

Acknowledgments: The work was supported by Researchers Supporting Project number (RSP2023R492), King Saud University, Riyadh, Saudi Arabia.

Appendix A

The data of the proposed systems are listed in the following Tables.

Table A1. Data of PV modules.

Parameter	**Technology**				
	Mono c-Si (Kyocera Solar PV120)	**Poly c-Si (Mitsubishi Electric PV-EE120MF5F)**	**Amorphous silicon, a-Si (Stion STN-120)**	**Cadmium Telluride, CdTe (First Solar Inc. FS-4120-3)**	**Copper Indium Selenium, CIS (Miasole Flex-03 120N)**
STC power (Wp)/panel	120	120.228	120	120.36	120.291
Number of cells	36	36	100	216	56
Open-circuit voltage (V)	21	21.6	53	88.7	37.8
Max voltage (Vmp) at MPP	16.9	17.2	40	70.8	30.1
Short-circuit current (A)	7.7	7.8	3.4	1.84	4.6
Max current (Imp) at MPP	7.1	7	3	1.7	4
Module area (m^2)	0.974	1.08	1.086	0.72	0.9
Series resistance (Ω)	0.2097	0.2566	2.3563	4.1584	0.905
Shunt resistance (Ω)	84.193	40.213	173.95	833.3934	69.95

Voltage temperature coefficient (mV/°C)	-0.377	-0.345	-0.316	-0.359	-0.241
Current temperature coefficient (%/°C)	0.055	0.064	0	0.073	-0.001
Power temperature coefficient (%/°C)	-0.504	-0.474	-0.383	-0.311	-0.361
Diode quality factor	0.965	0.95	0.80	0.6627	0.902
Module efficiency (%)	12.32	11.93	11.05	16.72	13.37

Table A2. Data of DC-DC boost converter.

Parameter	**Rating**
Input voltage	240-285 V
Output voltage	500 V
Switching frequency	5 kHz
L_1	0.45 mH
R_1	5 mΩ
C	12 mF

Table A3. Data of storage system.

Parameter	**Rating**
Type	Lithium-Ion
Nominal voltage	120 V
Rated capacity	800 Ah
Initial state of charge	50 %
Buck-boost-converter ratings	
L_2	0.10 mH
R_2	5 mΩ
Diodes of the buck-boost converter	
Internal resistor	1 mΩ
Snubber resistor	100 kΩ
Snubber capacitance	Inf

References

[1] E. Heydari, A. Y. Varjani, and D. Diallo, "Fast terminal sliding mode control-based direct power control for single-stage single-phase PV system," *Control Eng Pract*, vol. 104, p. 104635, 2020.

[2] Renewable Energy Policy Network for the 21st Century (REN21), "Renewables 2022 Global Status Report," 2022.

[3] K. N. Shukla, S. Rangnekar, and K. Sudhakar, "Mathematical modelling of solar radiation incident on tilted surface for photovoltaic application at Bhopal, MP, India," *International Journal of Ambient Energy*, vol. 37, no. 6, pp. 579–588, 2016.

[4] N. Karami, N. Moubayed, and R. Outbib, "General review and classification of different MPPT Techniques," *Renewable and Sustainable Energy Reviews*, vol. 68, pp. 1–18, 2017.

[5] P. Shaw, "Modelling and analysis of an analogue MPPT-based PV battery charging system utilising dc–dc boost converter," *IET Renewable Power Generation*, vol. 13, no. 11, pp. 1958–1967, 2019.

[6] Raiker Gautam A. and Loganathan Umanand, "Current Control of Boost Converter for PV interface with Momentum based Perturb and Observe MPPT," *IEEE Trans Ind Appl*, 2021.

[7] G. A. Ghazi *et al.*, "African Vulture Optimization Algorithm-Based PI Controllers for Performance Enhancement of Hybrid Renewable-Energy Systems," *Sustainability*, vol. 14, no. 13, p. 8172, 2022.

[8] Jately Vibhu, Azzopardi Brian, Joshi Jyoti, Sharma Abhinav, and Arora Sudha, "Experimental Analysis of hill-climbing MPPT algorithms under low irradiance levels," *Renewable and Sustainable Energy Reviews*, vol. 150, p. 111467, 2021.

[9] Nadeem Ahsan, Sher Hadeed Ahmed, and Murtaza Ali Faisal, "Online fractional open-circuit voltage maximum output power algorithm for photovoltaic modules," *IET Renewable Power Generation*, vol. 14, no. 2, pp. 188–198, 2020.

[10] Nadeem Ahsan, Sher Hadeed Ahmed., Murtaza Ali Faisal., and Ahmed Nisar, "Online current-sensorless estimator for PV open circuit voltage and short circuit current," *Solar Energy*, vol. 213, pp. 198–210, 2021.

[11] P. Verma, R. Garg, and P. Mahajan, "Asymmetrical interval type-2 fuzzy logic control based MPPT tuning for PV system under partial shading condition," *ISA Trans*, vol. 100, pp. 251–263, May 2020, doi: 10.1016/j.isatra.2020.01.009.

[12] Dehghani Majid, Taghipour Mohammad, Gharehpetian Gevork B, and Abedi Mehrdad, "Optimized fuzzy controller for MPPT of grid-connected PV systems in rapidly changing atmospheric conditions," *Journal of Modern Power Systems and Clean Energy*, vol. 9, no. 2, pp. 376–383, 2020.

[13] Eltamaly Ali M., Al-Saud M S., Abokhalil Ahmed G., and Farh Hassan M., "Simulation and experimental validation of fast adaptive particle swarm optimization strategy for photovoltaic global peak tracker under dynamic partial shading," *Renewable and Sustainable Energy Reviews*, vol. 124, p. 109719, 2020.

[14] R. S. Pal and V. Mukherjee, "Metaheuristic based comparative MPPT methods for photovoltaic technology under partial shading condition," *Energy*, vol. 212, p. 118592, 2020.

[15] Huang Yu-Pei, Huang Ming-Yi, and Ye Cheng-En, "A fusion firefly algorithm with simplified propagation for photovoltaic MPPT under partial shading conditions," *IEEE Trans Sustain Energy*, vol. 11, no. 4, pp. 2641–2652, 2020.

[16] Guo Ke, Cui Lichuang, Mao Mingxuan, Zhou Lin, and Zhang Qianjin, "An improved gray wolf optimizer MPPT algorithm for PV system with BFBIC converter under partial shading," *IEEE Access*, vol. 8, pp. 103476–103490, 2020.

[17] A. F. Mirza, M. Mansoor, K. Zhan, and Q. Ling, "High-efficiency swarm intelligent maximum power point tracking control techniques for varying temperature and irradiance," *Energy*, vol. 228, p. 120602, 2021.

[18] L. Gong, G. Hou, and C. Huang, "A two-stage MPPT controller for PV system based on the improved artificial bee colony and simultaneous heat transfer search algorithm," *ISA Trans*, Jun. 2022, doi: 10.1016/j.isatra.2022.06.005.

[19] Phanden Rakesh K., Sharma Lalit, Chhabra Jatinder, and Demir Halil İ., "A novel modified ant colony optimization based maximum power point tracking controller for photovoltaic systems," *Mater Today Proc*, vol. 38, pp. 89–93, 2021.

[20] Mosaad Mohamed I., abed el-Raouf M Osama, Al-Ahmar Mahmoud A., and Banakher Fahd A., "Maximum power point tracking of PV system based cuckoo search algorithm; review and comparison," *Energy Procedia*, vol. 162, pp. 117–126, 2019.

[21] Jamaludin Mohd N. *et al.*, "An effective salp swarm based MPPT for photovoltaic systems under dynamic and partial shading conditions," *IEEE Access*, vol. 9, pp. 34570–34589, 2021.

[22] D. Lamsal, V. Sreeram, Y. Mishra, and D. Kumar, "Smoothing control strategy of wind and photovoltaic output power fluctuation by considering the state of health of battery energy storage system," *IET Renewable Power Generation*, vol. 13, no. 4, pp. 578–586, 2019.

[23] B. Yang *et al.*, "Comprehensive overview of maximum power point tracking algorithms of PV systems under partial shading condition," *J Clean Prod*, vol. 268, p. 121983, 2020.

[24] A. T. Azar, F. E. Serrano, S. Vaidyanathan, and H. Albalawi, "Adaptive higher order sliding mode control for robotic manipulators with matched and mismatched uncertainties," in *International Conference on Advanced Machine Learning Technologies and Applications*, 2019, pp. 360–369.

[25] A. Merabet, L. Labib, A. M. Y. M. Ghias, C. Ghenai, and T. Salameh, "Robust feedback linearizing control with sliding mode compensation for a grid-connected photovoltaic inverter system under unbalanced grid voltages," *IEEE J Photovolt*, vol. 7, no. 3, pp. 828–838, 2017.

[26] F. Mohd Zaihidee, S. Mekhilef, and M. Mubin, "Robust speed control of PMSM using sliding mode control (SMC)—A review," *Energies (Basel)*, vol. 12, no. 9, p. 1669, 2019.

[27] F. Zhang, J. Maddy, G. Premier, and A. Guwy, "Novel current sensing photovoltaic maximum power point tracking based on sliding mode control strategy," *Solar Energy*, vol. 118, pp. 80–86, 2015.

[28] R. Garraoui, O. Barambones, M. ben Hamed, and S. Lassaad, "Real-time implementation of a maximum power point tracking algorithm based on first order sliding mode strategy for photovoltaic power systems," *Transactions of the Institute of Measurement and Control*, vol. 40, no. 5, pp. 1499–1509, 2018.

[29] M. R. Mostafa, N. H. Saad, and A. A. El-sattar, "Tracking the maximum power point of PV array by sliding mode control method," *Ain Shams Engineering Journal*, vol. 11, no. 1, pp. 119–131, 2020.

[30] R. Kumar M, S. Satya Narayana, and G. Vulasala, “Advanced sliding mode control for solar PV array with fast voltage tracking for MPP algorithm,” *International Journal of Ambient Energy*, vol. 41, no. 10, pp. 1192–1200, 2020.

[31] K. Dahech, M. Allouche, T. Damak, and F. Tadeo, “Backstepping sliding mode control for maximum power point tracking of a photovoltaic system,” *Electric Power Systems Research*, vol. 143, pp. 182–188, 2017.

[32] N. Chatrenour, H. Razmi, and H. Doagou-Mojarrad, “Improved double integral sliding mode MPPT controller based parameter estimation for a stand-alone photovoltaic system,” *Energy Convers Manag*, vol. 139, pp. 97–109, 2017.

[33] E. Heydari, A. Y. Varjani, and D. Diallo, “Fast terminal sliding mode control-based direct power control for single-stage single-phase PV system,” *Control Eng Pract*, vol. 104, p. 104635, 2020.

[34] Y. Zhu and J. Fei, “Adaptive global fast terminal sliding mode control of grid-connected photovoltaic system using fuzzy neural network approach,” *IEEE Access*, vol. 5, pp. 9476–9484, 2017.

[35] Q. Zhang, X. Zhuang, Y. Liu, C. Wang, and H. Guo, “A novel control strategy for mode seamless switching of PV converter in DC microgrid based on double integral sliding mode control,” *ISA Trans*, vol. 100, pp. 469–480, May 2020, doi: 10.1016/j.isatra.2019.12.013.

[36] A. Kchaou, A. Naamane, Y. Koubaa, and N. M’sirdi, “Second order sliding mode-based MPPT control for photovoltaic applications,” *Solar Energy*, vol. 155, pp. 758–769, 2017.

[37] A. Ziouh and A. Abbou, “Fuzzy-Super Twisting Sliding Mode MPPT Control for Three-Phase Grid-Connected PV,” *International Journal of Renewable Energy Research (IJRER)*, vol. 8, no. 4, pp. 1812–1823, 2018.

[38] A. Harrag and S. Messalti, “PSO-based SMC variable step size P&O MPPT controller for PV systems under fast changing atmospheric conditions,” *International Journal of Numerical Modelling: Electronic Networks, Devices and Fields*, vol. 32, no. 5, p. e2603, 2019.

[39] M. H. Qais, H. M. Hasanien, S. Alghuwainem, K. H. Loo, M. A. Elgendy, and R. A. Turky, “Accurate three-diode model estimation of photovoltaic modules using a novel circle search algorithm,” *Ain Shams Engineering Journal*, p. 101824, 2022.

[40] M. H. Qais, H. M. Hasanien, R. A. Turky, S. Alghuwainem, K.-H. Loo, and M. Elgendy, “Optimal PEM Fuel Cell Model Using a Novel Circle Search Algorithm,” *Electronics (Basel)*, vol. 11, no. 12, p. 1808, 2022.

[41] System Advisor Model Version 2022, “National Renewable Energy Laboratory.” Accessed: Sep. 27, 2022. [Online]. Available: https://sam.nrel.gov

[42] F. Belhachat and C. Larbes, “Modeling, analysis and comparison of solar photovoltaic array configurations under partial shading conditions,” *Solar Energy*, vol. 120, pp. 399–418, 2015.

[43] R. Ahmad, A. F. Murtaza, U. T. Shami, and F. Spertino, “An MPPT technique for unshaded/shaded photovoltaic array based on transient evolution of series capacitor,” *Solar Energy*, vol. 157, pp. 377–389, 2017.

[44] D. Xu, Q. Liu, W. Yan, and W. Yang, “Adaptive terminal sliding mode control for hybrid energy storage systems of fuel cell, battery and supercapacitor,” *Ieee Access*, vol. 7, pp. 29295–29303, 2019.

[45] A. Levant, “Sliding order and sliding accuracy in sliding mode control,” *Int J Control*, vol. 58, no. 6, pp. 1247–1263, 1993.

[46] A. Ammar, “Second-order sliding mode-direct torque control and load torque estimation for sensorless model reference adaptive system–based induction machine,” *Proceedings of the Institution of Mechanical Engineers, Part I: Journal of Systems and Control Engineering*, vol. 235, no. 1, pp. 15–29, 2021.

[47] B. Guo *et al.*, “A robust second-order sliding mode control for single-phase photovoltaic grid-connected voltage source inverter,” *IEEE Access*, vol. 7, pp. 53202–53212, 2019.

[48] J. A. Moreno and M. Osorio, “Strict Lyapunov functions for the super-twisting algorithm,” *IEEE Trans Automat Contr*, vol. 57, no. 4, pp. 1035–1040, 2012.

[49] Battery Supplies, “Lithium-Ion Batteries Cyclic Batteries Li-Ion.” Accessed: Sep. 27, 2022. [Online]. Available: https://batterysupplies.be/

[50] L. H. Saw, K. Somasundaram, Y. Ye, and A. A. O. Tay, “Electro-thermal analysis of Lithium Iron Phosphate battery for electric vehicles,” *J Power Sources*, vol. 249, pp. 231–238, 2014.

[51] C. S. Rao and S. Santosh, “Tuning optimal PID controllers for open loop unstable first order plus time delay systems by minimizing ITAE criterion,” *IFAC-PapersOnLine*, vol. 53, no. 1, pp. 123–128, 2020.

[52] M. H. Qais, H. M. Hasanien, R. A. Turky, S. Alghuwainem, M. Tostado-Véliz, and F. Jurado, “Circle Search Algorithm: A Geometry-Based Metaheuristic Optimization Algorithm,” *Mathematics*, vol. 10, no. 10, p. 1626, 2022.

[53] MathWorks Inc., “MathWorks Inc. MATLAB 2016b. 2016. Available online: https://www.mathworks.com/ (accessed on 1 June 2016).” Natick, Massachusetts, United States. [Online]. Available: https://www.mathworks.com/